Analysis of intermittency in turbulent flows by way of higher-order spectral moments

Samuel Lortie

Master of Science

Department of Mechanical Engineering

McGill University

Montreal, Québec, Canada

October 2021

A thesis submitted to McGill University in partial fulfillment of the requirements of the degree of Master of Science

ACKNOWLEDGEMENTS

First and foremost, I would like to express my sincere gratitude to my supervisor, Professor Laurent Mydlarski, for his patience, guidance, and support during the course of my degree. I am grateful for his encouragements and his enthusiasm for this research project. I would also like to thank Alaïs Hewes and Fanny Legay for teaching me how to use the equipment in the lab and Sheldon Harrison for helping me with my experiments. Additionally, I would like to thank the National Sciences and Engineering Research Council of Canada (NSERC) and the Fonds de recherche du Québec – Nature et technologies for funding my research. Finally, I would like to thank my wife, Mariane, and my parents, Diane and Marcel, for their continuous support throughout my degree.

ABSTRACT

The analysis of turbulence by way of higher-order spectral moments is uncommon, despite the relatively frequent use of such statistical analyses in other fields of physics and engineering. In this work, higher-order spectral moments are used to investigate the internal intermittency of the turbulent velocity and passive scalar (temperature) fields. This research first introduces the theory behind higher-order spectral moments as they pertain to the field of turbulence. Then, a short-time-Fourier-transform-based method is developed to estimate the higher-order spectral moments and provide a relative, scale-by-scale measure of intermittency. Experimental data are subsequently analysed and consist of measurements of homogeneous, isotropic, high-Reynolds-number, passive and active grid turbulence and wall-bounded turbulence (fully developed turbulent channel flow) over the Reynolds number range $35 \leq R_\lambda \leq 731$. Emphasis is placed on third- and fourth-order spectral moments using the definitions formalised by Antoni (2006), as such statistics are sensitive to transients and provide insight into deviations from Gaussian behaviour in grid turbulence. The higher-order spectral moments are also used to investigate the Reynolds and Péclet number dependence of the internal intermittency of velocity and passive scalar fields, respectively. The results demonstrate that the evolution of higher-order spectral moments with Reynolds number is strongly dependent on wavenumber. Additionally, the relative levels of internal intermittency of velocity and passive scalar fields are compared and a higher level of internal intermittency in the inertial subrange of the scalar field is consistently observed whereas a similar level of internal intermittency is observed for the velocity and passive scalar fields

for the high-Reynolds-numbers-cases as the Kolmogorov length scale is approached. Finally, higher-order spectral moments are shown to display increased levels in the near-wall region of a wall-bounded (channel) flow. The increased intermittent activity is believed to be caused by the presence of coherent structures in wall-bounded flows.

RÉSUMÉ

L'analyse d'écoulements turbulents au moyen de moments spectraux d'ordre supérieur est rare malgré l'utilisation relativement fréquente de ces statistiques dans d'autres domaines de la physique et de l'ingénierie. Des moments spectraux d'ordre supérieur sont utilisés dans cet ouvrage pour étudier l'intermittence interne des champs de vitesse turbulente et de scalaire passif (température). Cette étude offre d'abord une présentation de la théorie des moments spectraux d'ordre supérieur en les reliant à l'étude de la turbulence. Ensuite, une méthode basée sur la transformée de Fourier à court terme est développée pour estimer ces moments spectraux d'ordre supérieur et fournir une mesure relative de l'intermittence des écoulements turbulents échelle par échelle. Des données expérimentales sont ensuite analysées. Ces données consistent en des mesures en écoulements de turbulence homogène et isotrope et à nombres de Reynolds élevés. Ces écoulements sont créés à l'aide de grilles passives et actives et d'un canal à rapport hauteur-largeur élevé permettant d'atteindre des nombres de Reynolds dans l'intervalle $35 \leq R_\lambda \leq 731$. L'accent est mis sur les moments spectraux de troisième et quatrième ordres en utilisant les définitions présentées par Antoni (2006) car ces statistiques sont sensibles aux comportements transitoires et permettent de localiser les écarts au comportement gaussien des écoulements turbulents. Les moments spectraux d'ordre supérieur sont également utilisés pour étudier la dépendance qu'a l'intermittence interne des champs de vitesse et de scalaires passifs sur le nombre de Reynolds et de Péclet. Les résultats démontrent que le rythme auquel les moments spectraux d'ordre supérieur progressent grâce à l'évolution du

nombre de Reynolds dépend fortement du nombre d'onde. De plus, les niveaux relatifs d'intermittence interne des champs de vitesse et de scalaires passifs sont comparés et un niveau plus élevé d'intermittence interne est observé dans la zone inertielle des champs scalaires alors qu'un niveau similaire d'intermittence interne est observé pour les champs de vitesse et de scalaires passifs dans les cas où le nombre de Reynolds est élevé et pour des échelles s'approchant de celle de Kolmogorov. Enfin, une augmentation des valeurs des moments spectraux d'ordre supérieur est observée dans la région près de la paroi d'un écoulement en canal. L'augmentation de l'activité intermittente est expliquée par la présence de structures cohérentes dans les écoulements délimités par des parois.

TABLE OF CONTENTS

LIST OF TABLES

LIST OF FIGURES

CHAPTER 1
Introduction

1.1 Background and motivation

Fluid flows arise both in nature and in engineering practice. Understanding and predicting their behaviour is essential for many engineering applications, such as the flow of air around an airfoil, industrial pollutant dispersion into the environment, or fuel injection into a combustion chamber. Such flows are generally categorized as either "laminar" or "turbulent," with turbulent flows being the norm, whereas laminar flows are the exception. Flows in the laminar regime are characterised by parallel layers (or lamina) of fluid between which transfer of heat and momentum occurs primarily via molecular diffusion. Conversely, turbulent flows are characterised by chaotic and disordered motion.

Although no succinct definition of turbulence exists, turbulent flows share some common characteristics (Tennekes & Lumley, 1972). First, as noted above, turbulent flows have a chaotic, random and disordered behaviour, which arises from the nonlinear nature of the Navier-Stokes equations that govern fluid flow. Averaging each term in the Navier-Stokes equations yields (in tensor notation):

$$\frac{\partial \langle U_i \rangle}{\partial t} + \langle U_j \rangle \frac{\partial \langle U_i \rangle}{\partial x_j} = -\frac{1}{\rho}\frac{\partial \langle p \rangle}{\partial x_i} + \nu \frac{\partial^2 \langle U_i \rangle}{\partial x_j \partial x_j} - \frac{\partial \langle u_i u_j \rangle}{\partial x_j} \tag{1.1}$$

where U_i is the instantaneous velocity, u_i is the velocity fluctuation, t is time, x_j is the position, ρ is the density of the fluid, ν is the kinematic viscosity, and p is pressure. Equations 1.1 are often referred to as the Reynolds-Averaged Navier-Stokes (RANS)

equations. The last term on the right-hand-side has no equivalent in the original (non-averaged) Navier-Stokes equations and introduces new unknowns, although the number of equations remains the same. This is called the closure problem, and it makes the details of turbulence very difficult to predict, both analytically and numerically. Given the random and chaotic nature of turbulence, engineers and scientists rely on statistical methods to analyse turbulent flows. Moreover, turbulence has a strong ability to efficiently mix (or diffuse) quantities such as mass, momentum, and energy (e.g. heat). This yields increased mixing of substances, drag, and heat transfer rates. Furthermore, turbulence is a dissipative phenomenon and it needs a continuous energy supply to overcome the rapid viscous decay of turbulent energy. Finally, turbulence contains rotational structures (or "eddies") of varying scales that coexist and are superimposed. These common properties of turbulent flows are discussed extensively in the literature, and interested readers are referred to the works of Tennekes and Lumley (1972) and Pope (2000) for further details.

Turbulent flows arise from instabilities in laminar flows. The transition from laminar to turbulent flows is found to occur at large Reynolds numbers:

$$R = U\ell/\nu, \tag{1.2}$$

where U is a characteristic velocity in the flow field, and ℓ is a characteristic length scale. The Reynolds number can be interpreted as the ratio of inertial to viscous forces. As the Reynolds number is increased, the inertial forces increase in importance, such that the viscous forces become unable to dampen the instabilities, thus leading to the onset of turbulence. Moreover, turbulent flows may carry scalar contaminants (i.e. physical quantities such as temperature, humidity, chemical species

concentration). The mixing of scalar contaminants is an important sub-field of turbulence research, as it is relevant to many engineering applications such as pollutant dispersion and combustion. Note that a scalar field is deemed "passive" if its presence does not affect the turbulent velocity field.

As alluded to above, turbulence contains a wide range of scales. There is a continuum of scales that evolve in a so-called turbulent cascade. This cascade begins at the integral length scale (L), which is determined by the geometry of the flow and constitutes the largest length scale in the flow. The large scales then repeatedly break down into smaller eddies until the viscosity of the fluid eventually causes the kinetic energy of the smallest scales to be converted to internal energy. The small scales in turbulent flows are therefore bounded from below by the diffusive action of molecular viscosity. Moreover, small eddies have time scales that are much shorter then those of large eddies (Tennekes & Lumley, 1972). As a result, small scale structures should, in theory, be independent of the slower, large scale structures. This is one of the main ideas proposed by Kolmogorov (1941a, 1941b) in his pioneering theory of turbulence.

The continuum of length scales present in turbulent velocity and temperature fields is readily visualised by examining hot-wire anemometry and cold-wire thermometry signals, respectively shown in figures 1.1 (a) and (b). These time series show low frequency patterns of velocity and temperature fluctuations that evolve slowly over the entire length of time shown. These long fluctuations are created by the larger eddies in the flow. Conversely, rapid variations (over very short periods of time) are also observed in the velocity and temperatures signals. These are created by the smaller structures in the flow.

Time series of the (temporal) derivatives of the velocity fluctuations depicted in figure 1.1 (c) highlight another important characteristic of turbulence: turbulent

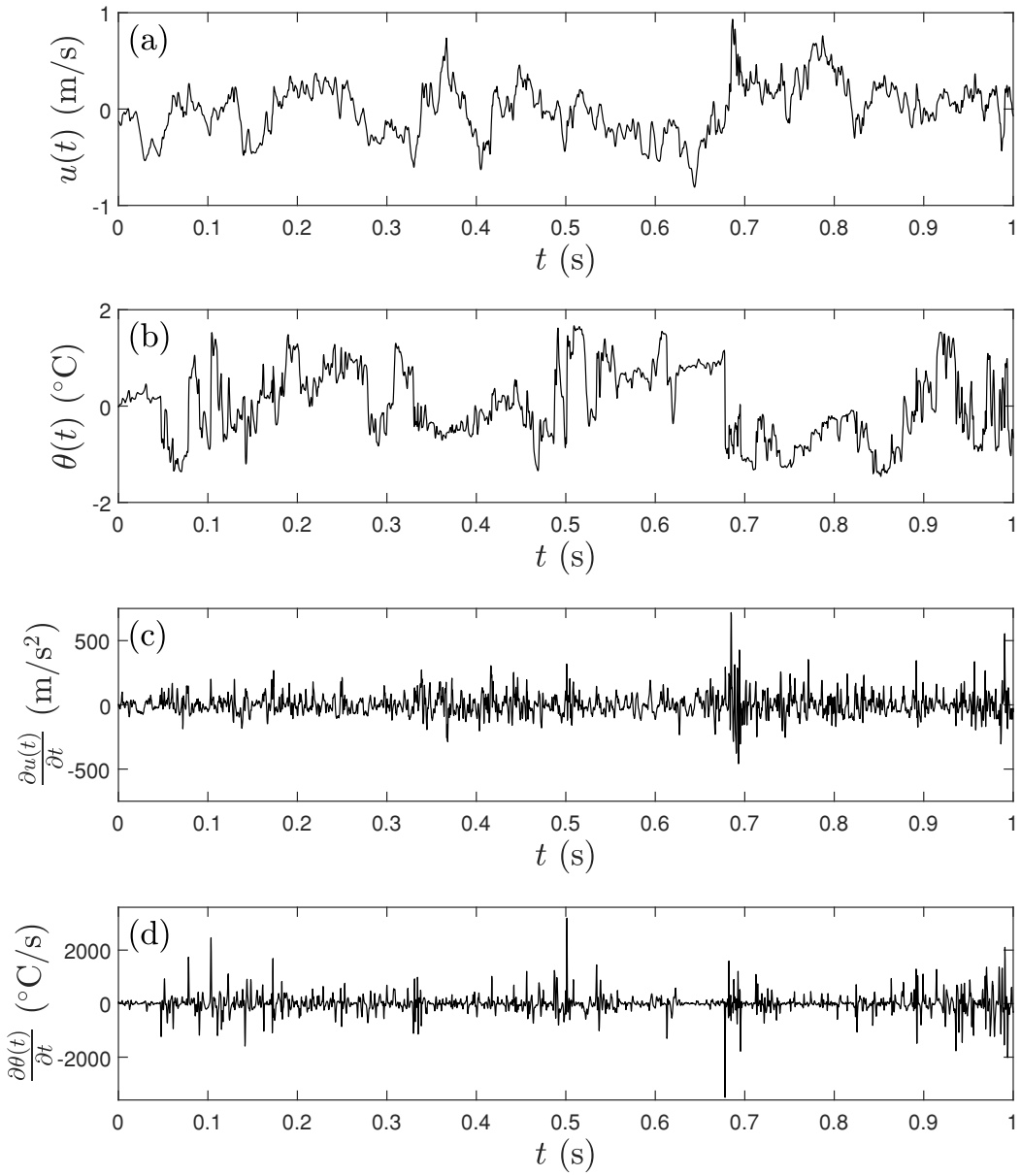

Figure 1.1: Time series of velocity and temperature fluctuations and their time derivatives measured in a wind tunnel by Mydlarski and Warhaft (1998).

flows are intermittent. The phenomenon is referred to as "internal intermittency" (for reasons that will become obvious shortly). Figure 1.1 (c) clearly shows periods of strong turbulent activity, interspersed with periods of relative quiescence. For reasons to be explained in §1.2, the velocity derivative relates to the small scales of turbulent flows, and the intermittent activity observed in figure 1.1 (c) is a reflection of the behaviour of the small scales in the flow (hence the term "internal" intermittency). Similar intermittent activity is observed in the passive scalar (temperature) fluctuation derivative depicted in figure 1.1 (d). However, note that this intermittent behaviour appears even more pronounced than that of the velocity field (figure 1.1 (c)). This simple, qualitative observation has lead to important research (Pumir, Shraiman, & Siggia, 1991; Holzer & Siggia, 1994; Warhaft, 2000), which qualitatively showed the higher level of internal intermittency of passive scalar fields and the independence of scalar-field intermittency from that of its advecting velocity fields.

Intermittency gives rise to a series of anomalous and irregular events that affect the statistics of turbulent flow fields. For example, figure 1.2 (a) shows the probability density function (PDF) of a turbulent velocity signal, which closely approximates that of a Gaussian distribution. However, one can observe that the PDF of the velocity derivative depicted in figure 1.2 (b) is non-Gaussian due to rare, intermittent events that populate the tails of this PDF. This implies that the PDF of the velocity field is also non-Gaussian despite appearing Gaussian (at large scales). The non-Gaussian behaviour of turbulence caused by the presence of internal intermittency is one of the aspects that make turbulent flows difficult to predict.

Given the issues that arise from the presence of internal intermittency, it follows that internal intermittency is a key element, and its understanding may bring

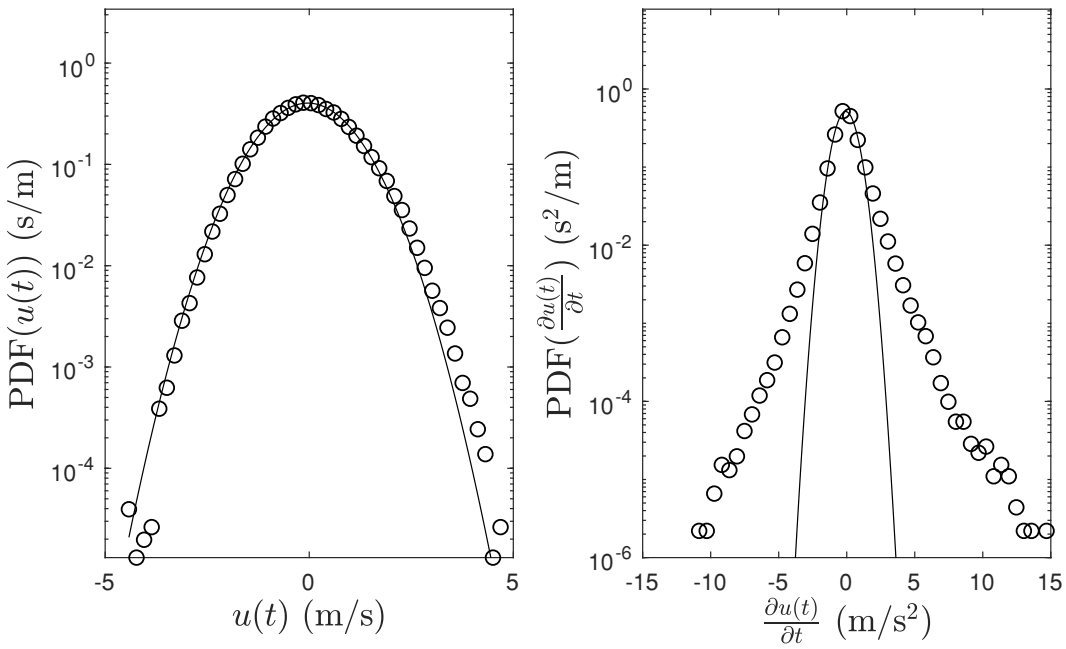

Figure 1.2: Probability density function of a velocity field and its time derivative. The solid black curves represent the best-fit Gaussian functions.

researchers closer to achieving a complete theory of turbulence, allowing more accurate predictions of the behaviour of turbulent flows. Advancing the understanding of internal intermittency (and thus, turbulent flows) is the main motivation behind the present work. This is done by way of higher-order spectral moments, which will be shown to not only allow the the detection of deviations from Gaussian behaviour in turbulent signals, but also to offer a better understanding of the evolution of these deviations across all length scales present in turbulent flows. Additionally, higher-order spectral moments are shown to have the ability to detect other intermittent phenomena present in turbulent flows that are not caused by internal intermittency (such as coherent structures in wall-bounded flows).

1.2 Literature Review

This section begins with an overview of research pertaining to turbulent flows, starting with the pioneering work of Kolmogorov. Then, a brief review of the literature pertaining to internal intermittency of turbulent flows is presented. Additionally, work done in other fields of physics and engineering to develop tools capable of detecting intermittent behaviour in signals is presented and their application to turbulence is discussed. Finally, the theory behind wall-bounded turbulent flows and their intermittent, coherent structures is summarised.

1.2.1 Kolmogorov theory of turbulence

The concept of a turbulent energy cascade originated from the work of Richardson (1922), who suggested that eddies of different sizes exist in turbulent flows. The instability of the larger eddies causes them to break down into smaller ones, and this process repeats until the smallest eddies in the flow lose their kinetic energy by viscous dissipation. As discussed in §1.1, the large-scale structures in turbulent flows depend on the geometry of the flow and thus depend on the type of flow. It is therefore impossible to universally describe large scales using a universal theory. However, the directional (and geometrical) biases of the large scales are lost as the eddies evolve down the turbulent cascade and break down into smaller, short-lived scales. Therefore, at sufficiently high Reynolds numbers, it has been argued that the turbulent motions of small scales become statistically isotropic. This observation suggests that small-scales could be characterized by a universal theory. This proposition, referred to as the postulate of local isotropy, was initially put forth by Kolmogorov (1941a, 1941b) (referred to herein as K41).

Starting from the postulate of local isotropy, K41 observed that the two dominant processes in the energy cascade were (i) the viscous dissipation of turbulent energy

at the smallest scales of the turbulent cascade, and (ii) the transfer of energy from large to small scales. K41 therefore suggested that small scales should only depend on (i) the kinematic viscosity of the fluid (ν), and (ii) the rate at which small scales in the flow are supplied with energy, which can be approximated by the rate at which small scales dissipate turbulent kinetic energy:

$$\langle \epsilon \rangle = 2\nu \langle s_{ij} s_{ij} \rangle, \tag{1.3}$$

where $s_{ij} = \frac{1}{2}\left(\frac{\partial u_i}{\partial x_j} + \frac{\partial u_j}{\partial x_i}\right)$ is the fluctuating strain rate. Given K41's proposition that the small scales only depend these two parameters, dimensional analysis yields:

$$\eta = f(\langle \epsilon \rangle, \nu) = \left(\frac{\nu^3}{\langle \epsilon \rangle}\right)^{1/4} \tag{1.4}$$

as a representation of the size of the smallest scales in turbulent flows. This length scale is referred to as the Kolmogorov length scale. This scaling applies to the small scales of turbulent flows (i.e. $\ell \ll L$) and the corresponding range of scales is referred to as the *dissipation range* (Pope, 2000).

Other length scales of turbulence have also been proposed. For example, in his study of isotropic turbulence, Taylor (1935) expressed the dissipation rate of turbulent kinetic energy as follows:

$$\langle \epsilon \rangle = \frac{15\nu \langle u^2 \rangle^{1/2}}{\lambda}. \tag{1.5}$$

He suggested that the length scale, λ, which is now known as the Taylor microscale, could be a representation of the dissipative scales of turbulence. However, this claim is debated, given that $\langle u^2 \rangle^{1/2}$ is not representative of the velocity scale of the eddies performing the dissipation. Moreover, it can be shown that the Taylor microscale is a length scales of intermediate size (i.e. $\eta < \lambda < L$). Despite not having a clear

physical interpretation, the Taylor microscale is often used in the study of turbulence. For example, it is regularly used as a length scale in the Taylor microscale Reynolds number:

$$R_\lambda = \frac{\langle u^2 \rangle^{1/2} \lambda}{\nu}, \tag{1.6}$$

which is used to quantify the intensity of turbulent flows.

In addition to his work on the small scales of turbulence, Kolmogorov also proposed the existence of an inertial subrange that separates the dissipative scales from the energy-containing (large-scale) ones, in the limit of sufficiently high Reynolds numbers (i.e. a range of scales, ℓ, such that $\eta \ll \ell \ll L$). This range expands as the Reynolds number is increased, resulting from the increased the separation of scales. K41 suggests that at high Reynolds numbers, this range, which is referred to as the *inertial subrange*, is large enough to not be influenced by viscosity nor the large scales of the turbulence, and the statistics of its motion are therefore only dependent on ϵ. Together, the dissipation range and the inertial subrange from the *universal equilibrium range*.

The consequences of the Kolmogorov theory of turbulence are also commonly noted when analysing the power spectral density of turbulent time series (referred to as the "spectrum" from here on):

$$E(\omega) = \frac{1}{2\pi} \int_{-\infty}^{\infty} R_\phi(\tau) d\tau, \tag{1.7}$$

where $R_\phi(\tau)$ is the autocovariance of any turbulent fluctuation. $E(\omega)$ is most often expressed in terms of wavenumber κ instead of frequency ω (see Pope (2000) for more details). If ϕ is the velocity fluctuation, $E(\kappa)$ represents the contribution to the turbulent kinetic energy from all wavenumbers. Appropriately normalising $E(\kappa)$

in the universal equilibrium range using Kolmogorov's theory, one obtains:

$$E(\kappa) = \langle\epsilon\rangle^{2/3}\kappa^{-5/3}F(\kappa\eta), \tag{1.8}$$

where $F(\kappa\eta)$ is a universal, non-dimensional function. It is therefore expected that the normalised power spectrum of all turbulent velocity fields collapse in the universal equilibrium range. This is supported by substantial experimental evidence (see, for example, Pope (2000) figure 6.14). Similarly, normalising the spectrum in the inertial subrange, one obtains:

$$E(\kappa) = C\langle\epsilon\rangle^{2/3}\kappa^{-5/3}, \tag{1.9}$$

where C is a constant. The wavenumber spectrum therefore follows a power law $E(\kappa) \sim \kappa^{-5/3}$ in the inertial subrange, which appears as a straight line of slope $-5/3$ when plotted in a log-log fashion. This is known as Kolmogorov's $-5/3$ law.

The pioneering work of Kolmogorov (1941a, 1941b), was later extended to passive scalar fields by Oboukhov (1949) and Corrsin (1951) (referred to herein as KOC theory), who proposed analogous concepts to those in K41, such as local isotropy of passive scalar fields and the existence of an inertial-convective subrange. Analogous to the concepts established by K41, KOC theory proposed that an important parameters of turbulent scalar fields is the rate of dissipation of the scalar variance, defined as:

$$\langle\epsilon_\theta\rangle = \gamma\left\langle\frac{\partial\theta}{\partial x_i}\frac{\partial\theta}{\partial x_i}\right\rangle, \tag{1.10}$$

where θ is the passive-scalar fluctuation and γ is the scalar molecular diffusivity.

The concept of the energy cascade was also extended to passive scalar fields by KOC, who analogously suggested the existence of a scalar field cascade. This cascade begins at the scalar integral length scale (L_θ) and ends at the smallest scale of the

scalar field (η_θ). As was the case with L, the size L_θ is dictated by the geometry of the flow. However, the size of the smallest eddies of a scalar fields is not only dependent on the kinematic viscosity of the fluid and the rate of dissipation of turbulent energy, but also on the diffusivity of the scalar (γ). If the scalar diffusivity is less than the kinematic viscosity (i.e. the Prandtl number ($\mathrm{Pr} = \nu/\gamma$) is greater than one), the scalar field is exposed to the entire spectrum of strain rate fluctuations and the smallest scalar eddies present in the flow scale as the "Batchelor scale":

$$\eta_\theta = \left(\frac{\nu\gamma^2}{\langle\epsilon\rangle}\right)^{1/4} = \eta\mathrm{Pr}^{-1/2}. \tag{1.11}$$

Conversely, if the scalar diffusivity is greater than the kinematic viscosity (i.e. $\mathrm{Pr} < 1$), the smallest scalar eddies are reprensented by the Corrsin scale:

$$\eta_\theta = \left(\frac{\gamma^3}{\langle\epsilon\rangle}\right)^{1/4} = \eta\mathrm{Pr}^{-3/4}. \tag{1.12}$$

Moreover, note that as a Prandtl number of one is approached ($\mathrm{Pr} \to 1$), the definitions of both the Batchelor and Corrsin scales suggest that η_θ approaches the Kolmogorov length scale (η).

1.2.2 Internal intermittency

As previously discussed, both the K41 and KOC theories make use of the mean dissipation rates ($\langle\epsilon\rangle$ and $\langle\epsilon_\theta\rangle$). However, it is now known that their instantaneous values (ϵ and ϵ_θ) exhibit strong variations in time and space (Landau, 1944; Sreenivasan & Antonia, 1997; Warhaft, 2000) — a phenomenon known as internal intermittency. Batchelor and Townsend (1949) were the first researchers to experimentally demonstrate the intermittency of turbulence, especially present at small scales. They differentiated a time series of velocity up to third order and demonstrated that the

signal became increasingly intermittent as the order of differentiation increased, observing periods of activity followed by periods of relative quiescence. They used the flatness factor of the velocity derivative:

$$F_n \equiv \frac{\langle (\partial^n u/\partial x^n)^4 \rangle}{\langle (\partial^n u/\partial x^n)^2 \rangle^2} \tag{1.13}$$

to quantify the extent to which the probability density function (PDF) of the velocity field deviated from that of a Gaussian distribution and observed a tendency of the flatness factor to increase with the order of differentiation (n). Kennedy and Corrsin (1961) subsequently demonstrated that the findings of Batchelor and Townsend (1949) were particular to turbulence by (experimentally and analytically) showing that this increase in flatness factor did not occur for all non-linear random processes. A subsequent theoretical study by Kraichnan (1967) suggested that the increased flatness factor (and intermittency) at the smallest scales of turbulence is explained by the rapid falloff of the spectrum at those scales, which causes slight fluctuations in the spectrum parameters to induce large changes in the velocity derivatives. Further work by Kuo and Corrsin (1971) attempted to locate the intermittency in wavenumber space by band-pass filtering turbulent signals and calculating the flatness factor within each band. They observed that the flatness (and thus the intermittency) increased when increasing the centre frequency of the band. They also found that the flatness tended to 3 at low wavenumbers, implying that the large scales of turbulence exhibited little intermittency. Additionally, they reinforced the idea that the degree of intermittency is Reynolds-number dependent by overlaying their results with those of Batchelor and Townsend (1949) and Wyngaard (1967), showing that the flatness factor (measured over all scales of the turbulence) increased with Reynolds number. Research in more recent years has suggested that

the flatness factor of the first derivative of the (longitudinal) velocity fluctuation increases monotonically with Reynolds number, possibly as $F_1 \sim R_\lambda^{3/8}$ (see Sreenivasan and Antonia (1997); Van Atta and Antonia (1980)), though more recent work by Djenidi, Antonia, and Tang (2019) claims that the flatness factor reaches a plateau at high Reynolds numbers. The intermittency of passive scalar fields has been subjected to less scrutiny, although data compiled by Sreenivasan and Antonia (1997) depict a stronger Reynolds-number dependence of the flatness factor of the scalar derivative than that of the longitudinal velocity derivative. Additionally, Sreenivasan and Antonia (1997) point out that the deviations from Gaussian behaviour of passive scalar fields are typically more significant than those of velocity fields, thus implying a stronger level of intermittency in scalar fields. It has moreover been demonstrated that intermittency in scalar fields can even occur when advected by (non-intermittent) Gaussian velocity fields (Holzer & Siggia, 1994; Kraichnan, 1994; Pumir et al., 1991). Warhaft (2000) also confirmed that the intermittent behaviour of passive scalar fields extends to scales larger than the dissipative ones, as is the case for velocity fields. Lepore and Mydlarski (2012) used the kurtosis of passive scalar increments ($\Delta\theta = [\theta(x + r) - \theta(x)]$) to study the evolution of intermittency with separation r and found that scalar fields exhibited significant departures from the Gaussian predictions for small and intermediate separations. However, it is worth noting that structure functions include contributions from all scales less than or equal to the scale r over which the increments are calculated (Meyer, Mydlarski, & Danaila, 2018).

1.2.3 Detection of intermittent behaviour

Although our understanding of internal intermittency has greatly improved with time, questions remain. For example, the scale dependence of internal intermittency

within velocity and/or passive scalar fields has not been extensively studied, even though the spectral nature of turbulent fields has been the object of much research. Spectral-based tools to detect bursts and transients have been used extensively in other fields of physics and engineering, especially in fault detection of rolling machines and bearings (see Antoni and Randall (2006), Leite et al. (2016), and Hu, Bao, Tu, Li, and Li (2019)). Another example is the use of higher- (i.e. third- and fourth-) order spectral moments to analyse acoustic signals contaminated by under-ice noise (Dwyer, 1983). Dwyer argued that conventional spectral analysis methods (such as power spectral densities) are incapable of detecting highly impulsive and non-Gaussian transients, and that higher-order spectral moments are more appropriate. He separately used the real and imaginary parts of the complex third- and fourth-order normalised moments (i.e. the spectral skewness and kurtosis) to identify transients of under-ice noise in the frequency domain. Pagnan and Ottonello (1994) later refined the technique and favoured the use of the magnitude of the complex fourth-order moment to obtain a more complete picture of the transients present in the signal.[1] Antoni (2006) subsequently undertook a more rigorous derivation of the properties of the spectral kurtosis, demonstrating that this higher-order moment is particularly well-suited for the detection of transients in a signal. However, he also demonstrated that care must be taken in constructing an appropriate estimation method that favours the detection of short transients. With a few exceptions, such approaches have generally not been applied to turbulent flows, which are nonetheless both spectral and intermittent in nature. Successful attempts at isolating deviations

[1] When using this method, however, one must be aware of the change of expected distributions due to the squaring operations necessary to obtain the magnitude of the complex Fourier modes.

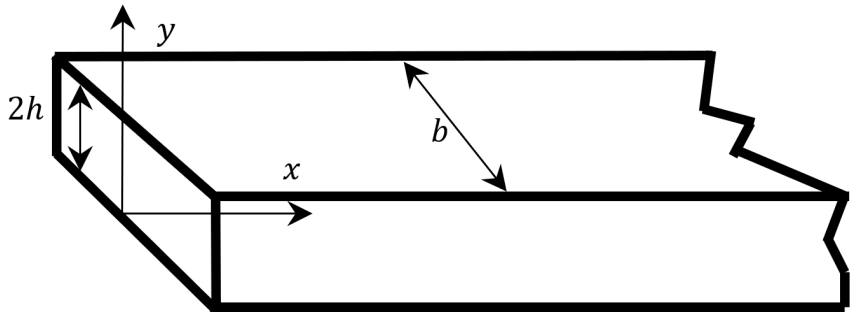

Figure 1.3: Sketch of a high-aspect ratio channel.

from Gaussian behaviour in wavelet space have been presented by Meneveau (1991) and Farge (1992), though these studies only considered the behaviour of velocity fields (without passive scalars) and limited their analysis to wavelet decomposition, as opposed to the more common Fourier analysis. The use of fourth-order moments in the Fourier domain for the analysis of turbulence was investigated by Chevillard, Mazellier, Poulain, Gagne, and Baudet (2005), who calculated the flatness factor of experimental velocity data in the frequency domain to demonstrate the higher level of intermittency of vorticity compared to longitudinal velocity.

1.2.4 Review of wall-bounded flows and their coherent strucutures

Wall-bounded shear flows (e.g. internals flows and boundary layers) are thoroughly discussed in Tennekes and Lumley (1972) and Pope (2000). This research make use of the a high-aspect-ratio channel described in §3.2.1 to study the intermittent behaviour of bounded turbulent flows.

A visual representation of the channel used for this research is shown in figure 1.3. For fully-developed, high-aspect-ratio flows, the velocity only varies in the y-

direction, meaning that the continuity equation reduces to

$$\frac{\partial \langle V \rangle}{\partial y} = 0, \tag{1.14}$$

which implies that the average wall-normal velocity ($\langle V \rangle$) does not vary in the y-direction. Since the no slip condition must be satisfied, the wall-normal velocity at the wall must be zero, thus implying that $\langle V \rangle = 0$ everywhere in the flow. For turbulent channel flow, the equation of conservation of y-momentum (equation 1.1 with $i = 2$) reduces to:

$$\frac{-1}{\rho}\frac{\partial \langle p \rangle}{\partial y} - \frac{d}{dy}\langle V^2 \rangle = 0, \tag{1.15}$$

which, if integrated in y and differentiated in x, shows that the pressure gradient along the x direction is constant ($\frac{\partial \langle p \rangle}{\partial x} = \frac{dp_{wall}}{dx}$). Similarly, the equation of conservation of x-momentum (equation 1.1 with $i = 1$) reduces to:

$$\frac{-1}{\rho}\frac{\partial \langle p \rangle}{\partial x} - \frac{d}{dy}\langle uv \rangle + \nu\frac{d^2\langle U \rangle}{dy^2} = 0, \tag{1.16}$$

which can be integrated in y (from $y = 0$ to y) to yield

$$\frac{-y}{\rho}\frac{\partial \langle p \rangle}{\partial x} - \langle uv \rangle + \nu\left[\frac{d\langle U \rangle}{dy}\right]_{y=0}^{y=y} = 0. \tag{1.17}$$

Using the fact that $\frac{\partial \langle p \rangle}{\partial x} = \frac{dp_{wall}}{dx}$ and rearranging, one obtains:

$$-\langle uv \rangle + \nu\frac{d\langle U \rangle}{dy} = u_\tau^2\left(1 - \frac{y}{h}\right), \tag{1.18}$$

where $u_\tau = \left(\frac{-h}{\rho}\frac{dp_{wall}}{dx}\right)^{1/2}$ is the friction velocity. Equation 1.18 can be solved by appropriately non-dimensionalizing it for each region of the flow. The regions of the flow are determined using the viscous length scale $\delta_\nu = \nu/u_\tau$ and non-dimensional parameter $y^+ = y/\delta_\nu$.

In the *near wall region* ($y^+ < 50$), the length scale is viscosity-dominated because of the proximity with the wall where the no-slip condition must be satisfied. Non-dimensionalizing equation 1.18 using viscous scaling and assuming a high Reynolds number yields:

$$-\frac{\langle uv \rangle}{u_\tau^2} + \frac{du^+}{dy^+} = 1, \tag{1.19}$$

where $u^+ = \langle U \rangle / u_\tau$. For a smooth wall, this suggests that $u^+ = f(y^+)$ and $\frac{\langle uv \rangle}{u_\tau^2} = g(y^+)$, meaning that u^+ only depends on y^+. This is often refered to as the *Law of the Wall*. Very close to the wall, there exists a viscous sublayer, where the Reynolds stress from equation 1.19 can be neglected. The viscous sublayer begins at the wall and has (experimentally) been shown to end at $y^+ = 5$. In this region, the first term of equation 1.19 disappears. Solving the simplified equation, one obtains:

$$\langle U \rangle / u_\tau = y^+, \tag{1.20}$$

such that in the viscous sublayer, the mean velocity to varies linearly with distance from the wall.

Flow visualisations in the near wall-region (e.g. Kline, Reynolds, Schraub, and Runstadler (1967)) have revealed the existence of turbulent coherent structures in wall-bounded flows. In the near-wall region, experiments have shown structures called *streaks*, which are thin layers of slow-moving fluids enclosed between layers of faster-moving fluid (Pope, 2000). These structures, which are observed in the region $y^+ < 40$, have a characteristic behaviour called *bursting*. This phenomenon occurs as the streaks migrate in the streamwise direction and slowly move away from the wall. The streaks eventually undergo a process called *streak lifting* during which the streaks are rapidly ejected from the wall, oscillate, and break down into

smaller-scales (Pope, 2000). This process is distinct from the mechanisms that cause internal intermittency, but it is nevertheless a cyclic and highly intermittent process Robinson (1991). Detailed discussion of streaks are available in Pope (2000) and Robinson (1991). The increased intermittent activity caused by streaks is further investigated in chapter 4 by way of higher-order spectral moments.

In the *outer layer* ($y^+ > 50$) of wall bounded flows, viscous effects are negligible. Thus, we non-dimensionalize equation 1.18 using outer scaling: y/h. Assuming a high Reynolds number, equation 1.18 becomes:

$$-\frac{\langle uv \rangle}{u_\tau^2} = 1 - y/h. \tag{1.21}$$

This gives no information regarding the mean velocity. However, scaling of the kinetic energy budget give rises to the *Velocity Defect Law*:

$$\frac{\langle U \rangle - U_0}{u_\tau} = F(y/h). \tag{1.22}$$

In the *inertial sublayer*, the Law of the Wall and the Velocity Defect Law are asymptotically matched by taking the limit as $y^+ \to \infty$ and $y/h \to 0$. The Law of the Wall can be written as:

$$\frac{d\langle U \rangle}{dy} = \frac{u_\tau^2}{\nu} \frac{df(y^+)}{dy^+}, \tag{1.23}$$

and the Velocity Defect Law can be written as:

$$\frac{d\langle U \rangle}{dy} = \frac{u_\tau}{h} \frac{dF(y/h)}{d(\frac{y}{h})}, \tag{1.24}$$

such that both equations can be equated, yielding:

$$\frac{u_\tau}{h} \frac{dF(y/h)}{d(\frac{y}{h})} = \frac{u_\tau^2}{\nu} \frac{df(y^+)}{dy^+}. \tag{1.25}$$

Given that F is a function of y/h only and f is a function of y^+ only, all sides of equation 1.25 must be equal to the same universal constant denoted by $1/\kappa$. Integrating equation 1.25 yields:

$$\frac{\langle U \rangle - U_0}{u_\tau} = \frac{1}{\kappa} \ln(y/h) + B \tag{1.26}$$

and

$$\frac{\langle U \rangle}{u_\tau} = \frac{1}{\kappa} ln(y^+) + A, \tag{1.27}$$

where $\kappa = 0.41 \pm 5\%$, $A = 5.2 \pm 5\%$, and B is flow-dependent. Equation 1.27 is refered to a the *Log Law* and describes the behaviour of the mean flow in the range bounded by $y^+ = 30$ and $y/h = 0.3$.

1.3 Objectives

As previously discussed, the intermittent behaviour of turbulent flows is an important element that makes turbulence difficult to predict. Therefore, fully understanding internal intermittency and other forms of transient behaviour in turbulent flows is a key element that may bring researchers closer to achieving a complete theory of turbulence. Although researchers' understanding of internal intermittency has greatly improved as a result of the research work discussed in §1.2.2, questions remain. For example, the evolution of the intermittency across the frequency/wavenumber domain has not been extensively studied. However, tools that make use of the third- and fourth-order moments in the frequency domain to detect and situate intermittency have been developed in other fields of physics and engineering and these tools can be used to study the scale-by-scale evolution of intermittency in turbulent flows.

Given the above, the objective of the present study is fourfold. The first objective is to investigate internal intermittency in turbulent flows by way of third- and

fourth-order spectral moments. To do so, a short-time-Fourier-transform- (STFT-) based method (similar to that of Antoni (2006)) that makes use of higher-order spectral moments to quantify the internal intermittency in the frequency/wavenumber domain is developed. The proposed tool (i) does not necessitate band-pass filtering of time series of data, (ii) permits the investigation of internal intermittency as a function of frequency/wavenumber, and (iii) allows the possibility of variable window lengths (discussed in later sections), akin to the analysis of Antoni (2006). The second objective is to make use of higher-order spectral moments to explore the Reynolds-number dependence of the internal intermittency of both velocity and scalar fields. The third is to compare the intermittency of both velocity and passive scalar fields on a spectral basis. Finally, the fourth objective is to investigate the use of higher-order spectral moments in wall-bounded flows by comparing the levels of intermittent activity at different wall-normal locations in a turbulent channel flow.

1.4 Structure of thesis

The remainder of this thesis addresses the objectives outlined in §1.3, beginning with an overview of the mathematical background of higher-order spectral moments in chapter 2. This chapter also includes the development of a higher-order spectral moments estimation method tailored to the study of turbulence, as well as some test cases to validate the estimation method. This is followed in chapter 3 with a discussion of the experimental apparatus and data acquisition procedures. The results obtained in grid turbulence are given in the first part of chapter 4, where an overview and comparison the evolution of the internal intermittency of velocity and passive scalar fields is presented. Results obtained in a turbulent channel flow are presented in the second part of chapter 4, to compare the intermittency observed

in homogeneous, isotropic turbulence with that in a wall-bounded flow. Finally, concluding remarks and suggestions for future work are given in chapter 5.

CHAPTER 2
Theory and implementation of higher-order spectral moments

As noted in chapter 1, higher-order spectral moments are seldom used in fluid mechanics, though they are encountered much more commonly in other fields of physics and engineering. Similar tools are used herein to detect non-stationary behaviour in turbulent signals caused by internal intermittency. This section begins with a presentation of the mathematical background necessary to calculate higher-order spectral moments. It is followed by a discussion of the method used to analyse time series of turbulent velocity and passive scalar fields.

2.1 Mathematical background

The mathematical background behind higher-order spectral moments is given in this section, beginning with the mathematical definitions adapted from the work of Dwyer (1983) and Antoni (2006). This is followed by a discussion of certain consequences of the mathematical operations carried out to calculate higher-order spectral moments.

2.1.1 Definition of higher-order spectral moments

Let a continuous process $x(t)$ be sampled at a frequency f_s. The resulting discrete time series can then be divided into M segments of length N (via the use of windowing functions, which will be discussed in depth in §2.2.1), such that the sampled time series can be denoted as:

$$x(t) = x([n + N(m-1)]/f_s), \tag{2.1}$$

with $n = 0, \ldots, N-1$ and $m = 1, \ldots, M$. The discrete Fourier transform (DFT) of each individual segment (denoted by m) is then calculated as follows:

$$X(\omega_n, m) = \sum_{k=0}^{N-1} x(k, m) e^{jkn/N}, \tag{2.2}$$

where $j = \sqrt{-1}$ and $\omega_n = 2\pi n f_s / N$. Note that this operation is normally performed using the fast Fourier transform (FFT) algorithm. The power spectrum is calculated from the average of the square of the modulus of $X(\omega_n, m)$, evaluated at each frequency bin (centred at ω_n), over each segment of length M:

$$E(\omega_n) = \frac{1}{f_s M} \sum_{m=1}^{M} |X(\omega_n, m)|^2, \tag{2.3}$$

where the factor $1/f_s$ is necessary, such that:

$$\langle x^2 \rangle = \int_{-\infty}^{\infty} E(\omega_n) d\omega_n. \tag{2.4}$$

This segmenting and averaging method has multiple advantages, including a reduction in the number of computations required (since it is more efficient to take the FFT of multiple short segments than taking the FFT of the equivalent longer segment) and a lower noise level (Welch, 1967).

Though the power spectrum is used extensively in the study of turbulence to compare the relative intensity of the fluctuations at the various scales of the turbulence, it fails to capture the non-stationary behaviours induced by internal intermittency because it is not very sensitive to the tails of the distribution of a signal (Dwyer, 1983; Kuo & Corrsin, 1971). The spectrum is therefore not well suited for situating intermittency in wavenumber space. As previously noted, attempts to experimentally filter velocity signals using narrow bands to locate intermittency in wavenumber

space have been made (e.g. Kuo and Corrsin (1971)), but there exists a simple, flexible (in terms of frequency bin resolution) and rigorous alternative that employs the frequency-domain signal $X(\omega_n, m)$ to locate and quantify intermittency in the frequency/wavenumber domain. This method makes use of higher-order spectral moments, which are able to capture deviations from Gaussian behaviour in the tails of the PDFs. By viewing the N segments of data created from the signal $x(t)$ as independent observations, one can create a PDF of the spectral coefficients at each frequency bin, and then define the spectral skewness, $\tilde{S}$:

$$\tilde{S}(\omega_n) = \frac{\frac{1}{M}\sum_{m=1}^{M} |X(\omega_n, m)|^3}{\left(\frac{1}{M}\sum_{m=1}^{M} |X(\omega_n, m)|^2\right)^{3/2}}, \tag{2.5}$$

and the spectral kurtosis, $\tilde{K}$:

$$\tilde{K}(\omega_n) = \frac{\frac{1}{M}\sum_{m=1}^{M} |X(\omega_n, m)|^4}{\left(\frac{1}{M}\sum_{m=1}^{M} |X(\omega_n, m)|^2\right)^{2}}, \tag{2.6}$$

as the normalised third- and fourth-order moments of the frequency-domain PDFs. Note that tildes denote spectral moments in this work.

2.1.2 Distribution of Fourier modes

The definitions for the spectral skewness and kurtosis given in §2.1.1 differ slightly from those of the spectral skewness and kurtosis presented by Dwyer (1983), which separately employed the real and imaginary parts of the Fourier-transformed signal ($X^r(\omega_n, m)$ and $X^i(\omega_n, m)$, respectively), producing pairs of spectral moments that must be analysed individually. For a stationary Gaussian process, a spectral skewness of 0 and a spectral kurtosis of 3 are to be expected with Dwyer's method. However, the aforementioned revised definitions of $\tilde{S}(\omega_n)$ and $\tilde{K}(\omega_n)$, given by Pagnan and Ottonello (1994) and Antoni (2006), employ the *modulus* of the Fourier

transform (equations (2.5) and (2.6)), to simplify each spectral moment to a single parameter. Use of the magnitude of the complex, Fourier-transformed variables changes the nature of their distribution such that Gaussian statistics would give rise to a chi distribution, with the following probability density function (Forbes, Evans, Hastings, & Peacock, 2011):

$$f(X, \sigma, L) = \frac{2^{1-L/2} X^{L-1}}{\Gamma(L/2)\sigma^L} \mathrm{e}^{-X^2/2\sigma^2}, \tag{2.7}$$

where L is the degree of freedom ($L = 2$ for the magnitude of complex numbers), σ is the standard deviation of $X^r(k,l)$ and $X^i(k,l)$, and Γ is the gamma function. (See Millioz, Huillery, and Martin (2006) for more details.) The raw moments of the chi distribution can thus be calculated from:

$$\mu_j = \langle X^j \rangle = \int_{-\infty}^{\infty} X^j \frac{2^{1-L/2} X^{L-1}}{\Gamma(L/2)\sigma^L} \mathrm{e}^{-X^2/2\sigma^2} dX, \tag{2.8}$$

which reduces to (see Appendix A for the detailed derivation):

$$\mu_j = \sigma^j 2^{j/2} \frac{\Gamma(\frac{1}{2}(L+j))}{\Gamma(\frac{1}{2}L)}. \tag{2.9}$$

Therefore, if the signal $x(t)$ is stationary and Gaussian, the definitions proposed in equations (2.5) and (2.6) lead to a spectral skewness of (see Appendix A):

$$\tilde{S} = \frac{\mu_3}{\mu_2^{3/2}} = \Gamma(5/2) \approx 1.33, \tag{2.10}$$

and a spectral kurtosis of:

$$\tilde{K} = \frac{\mu_4}{\mu_2^2} = 2. \tag{2.11}$$

The present work employs the modulus in the definition of higher-order spectral moments because of its simplicity. It should therefore be recalled that, at a given

scale, and if the signal is Gaussian, the third- and fourth-order spectral moments of a turbulent velocity or scalar field will take on the values of 1.33 and 2, respectively, at that particular scale.

2.2 Estimation of higher-order spectral moments

This section focuses on the development and testing of a method to estimate the higher-order spectral moments of discrete time series. It begins with an overview of the chosen estimation algorithm, followed by a discussion of issues that arise with the segmentation (or windowing) of discrete time series. Finally, it presents validation test cases and their results.

2.2.1 Short-time-Fourier-transform-based algorithm

The higher-order spectral moment estimation method proposed herein makes use of window functions to create multiple sets of data from a time series $x(t)$. The creation of segments proposed in equation (2.1) is equivalent to the application of a square window and therefore results in considerable amounts of spectral leakage due to the non-negligible sidelobes present in the Fourier transform of the square window. The use of a symmetrical window function that gradually decreases to zero at either end, such as the Hann window, is preferable as it reduces spectral leakage (Press et al., 1986). In practice, we therefore multiply the signal under investigation by a window function $w(k)$ before the taking the Fourier transform, such that equation (2.2) becomes:

$$X(\omega_n, m) = \sum_{k=0}^{N-1} w(k)x(k, m)e^{jkn/N}. \tag{2.12}$$

This method, often referred to as the short-time Fourier transform (STFT), approximates the spectral content of the signal around the time where the window function is centred. Though the time at which a given spectral event occurs may not be of

immediate interest in the analysis of internal intermittency, the repeated extraction of spectral content done by taking the STFT at different times in the signal $x(t)$ creates a distribution in the frequency domain from which one can extract the third- and fourth-order moments.

Though this method allows the extraction of higher-order statistical moments in the frequency domain, the evolution of statistical moments in space is also of great interest. Fortunately, there exists a technique to approximate spatial measurements from single-point, temporal measurements (i.e. measurements taken using a single, stationary probe). This method, known as Taylor's Frozen Flow Hypothesis, uses the fact that the turbulence does not appreciably change during the measurement period when in the presence of a strong mean flow, such that one can estimate the spatial power spectrum ($F_{11}(f)$) from the frequency power spectrum ($F_{11}(\omega)$) via the following approximations (Lumley, 1965):

$$F_{11}(\kappa_1) = \frac{\langle U \rangle}{2\pi} F_{11}(f) \tag{2.13}$$

and

$$\kappa_1 = \frac{2\pi}{\langle U \rangle} f. \tag{2.14}$$

The accuracy of this method depends on the intensity of the turbulence. Research has shown that the approximation generally yields valid results if $\langle u^2 \rangle^{1/2} / \langle U \rangle \ll 1$ (Pope, 2000). This is shown to be the case for the data used herein in Chapter 3.

2.2.2 Windowing issues

Despite its ability to extract the spectral content of a signal and identify frequencies at various points in time, the STFT has certain limitations. The results depend (to a certain extent) on the smoothness of the chosen windowing function,

though this dependence was not observed to be strong enough to influence the conclusions presented in later sections. A preliminary analysis (not shown) that compared the Blackman, Chebyshev, Gaussian, Hann (used herein), and rectangular windows demonstrated that similar results are obtained when any windowing function is used, apart from the rectangular one. Substantial research (e.g. Press et al. (1986)) has shown that the use of rectangular windows leads to significant spectral leakage, which is the main reason it is not used herein. Of the four windowing functions that gave similar results, the Hann window was favoured for the sake of consistency between the present research and previous work done on higher-order spectral moments (e.g. Antoni 2006).

The results of the STFT method are affected by the windowing process. To illustrate this, consider the turbulent time series of velocity shown in figure 2.1(a). The largest wavelength (lowest frequency) that the windowing function (dashed line in figure 2.1) can resolve corresponds to the width of the window itself. Therefore, any frequency lower than the frequency corresponding to the filtering window's length cannot be resolved. One solution to this issue is to increase the width of the filtering window (figure 2.1(c)). However, as the width of the window increases, issues related to the Central Limit Theorem arise. Specifically, Peligrad and Wu (2010) have demonstrated that for ergodic processes and for large enough sample sizes, the Central Limit Theorem holds for Fourier transforms. Thus, if a windowed Fourier transform is performed, one should expect the length of the window (N) to influence the distribution of the Fourier transformed data. This is readily demonstrated by considering a hypothetical random variable $x(t)$ and its sampled time series $x(n, m)$. The time series has a skewness of 0 and a kurtosis of 2.5, such that its PDF is not Gaussian. A windowed STFT, with window lengths ranging from

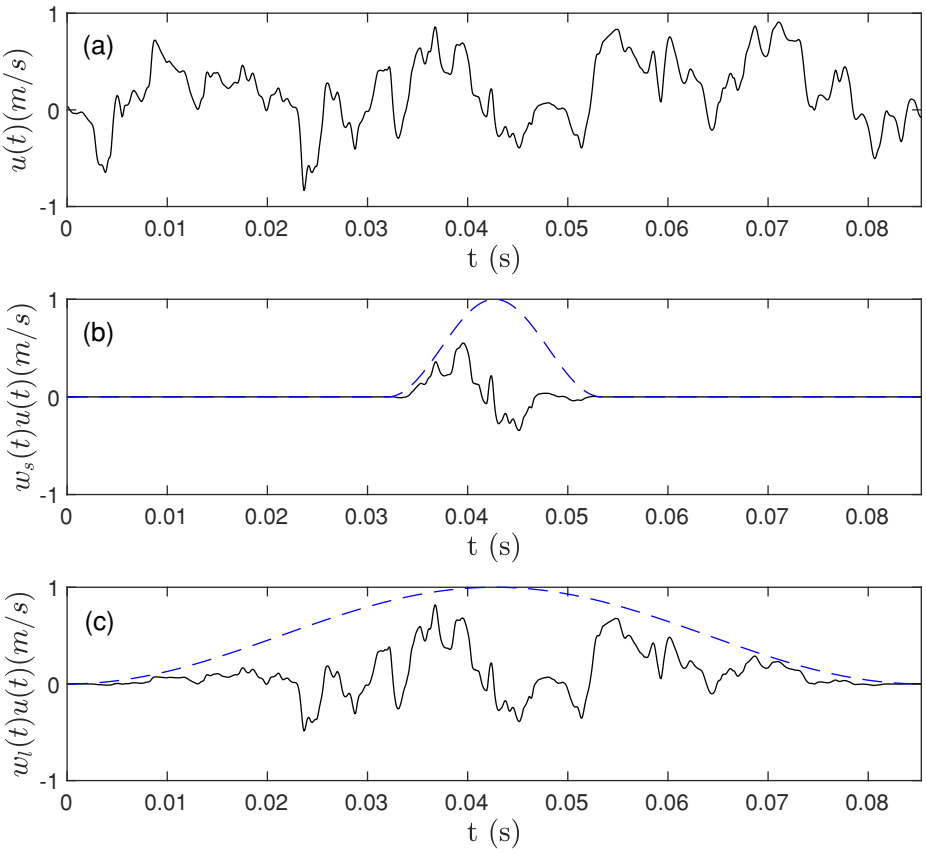

Figure 2.1: A turbulent velocity time series (−) with window functions (−−) applied. (a) The original velocity signal, (b) the velocity signal with a short window applied, and (c) the velocity signal with a long window applied.

$N = 2^2$ to $N = 2^9$, was performed on this time series, giving rise to the complex random variable $X(\omega_n, m)$. The mean of the kurtosis of this random variable (taken over all frequency bins) was then calculated, first considering only $X^r(\omega_n, m)$ (i.e. the real part of $X(\omega_n, m)$):

$$\langle \tilde{K}^r(\omega_n) \rangle = \left\langle \frac{\frac{1}{M}\sum_{m=1}^{M} X^r(\omega_n, m)^4}{\left(\frac{1}{M}\sum_{m=1}^{M} X^r(\omega_n, m)^2\right)^2} \right\rangle, \tag{2.15}$$

then only $X^i(\omega_n, m)$ (i.e. the imaginary part of $X(\omega_n, m)$):

$$\langle \tilde{K}^i(\omega_n) \rangle = \left\langle \frac{\frac{1}{M}\sum_{m=1}^{M} X^i(\omega_n, m)^4}{\left(\frac{1}{M}\sum_{m=1}^{M} X^i(\omega_n, m)^2\right)^2} \right\rangle, \tag{2.16}$$

and finally $|X(\omega_n, m)|$ (i.e. the magnitude of $X(\omega_n, m)$):

$$\langle \tilde{K}(\omega_n) \rangle = \left\langle \frac{\frac{1}{M}\sum_{m=1}^{M} |X(\omega_n, m)|^4}{\left(\frac{1}{M}\sum_{m=1}^{M} |X(\omega_n, m)|^2\right)^2} \right\rangle, \tag{2.17}$$

which is simply the mean of the spectral kurtosis defined in equation (2.6). The evolution of these quantities as a function of window length is depicted in figure 2.2, which depicts how the kurtosis is influenced by the window length. As the window length tends to one ($N \to 1$), the platykurtic character of the original time series forces $\langle \tilde{K}^r(\omega_n) \rangle$ and $\langle \tilde{K}^i(\omega_n) \rangle$ to decrease towards the value of the kurtosis of the original time series (2.5). Conversely, as the window length increases toward infinity ($N \to \infty$), $\langle \tilde{K}^r(\omega_n) \rangle$ and $\langle \tilde{K}^i(\omega_n) \rangle$ approach the Gaussian value of 3, even though the original time series $x(n, m)$ was non-Gaussian. This is a result of the Central Limit Theorem which states that, for a large enough sample size, the distribution of the sample mean (or sample Fourier Transform) becomes Gaussian regardless of the original distribution. Note that the behaviour of $\langle \tilde{K}(\omega_n) \rangle$ is similar, though it does not tend to the value of the kurtosis of the original time series (2.5) as $N \to 1$ because of the aforementioned change in distribution resulting from the squaring operation inherent in the calculation of the magnitude. Moreover, as $N \to \infty$, $\langle \tilde{K}(\omega_n) \rangle$ tends to the value of 2 instead of 3, for the reasons discussed in §2.1.

Having established that higher-order spectral moments estimated with large windows cannot be used to detect intermittency due to the Central Limit Theorem, one must also recognize that excessively short windows fail to capture low frequency

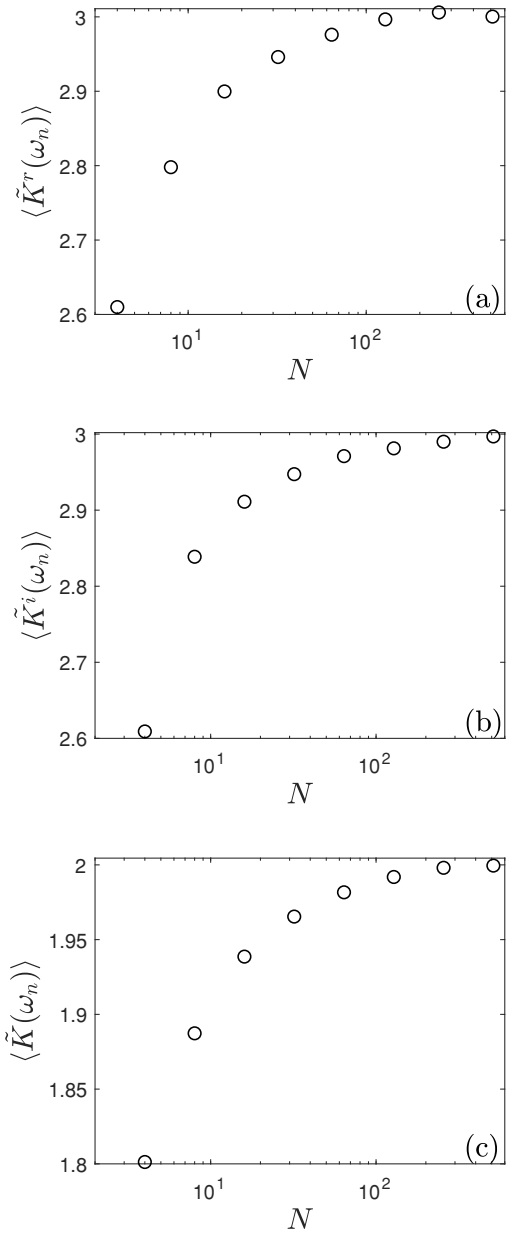

Figure 2.2: The mean spectral kurtosis plotted as a function of the window length (N) for (a) the real part of $X(\omega_n, m)$, (b) the imaginary part of $X(\omega_n, m)$, and (c) the magnitude of $X(\omega_n, m)$.

transients. Therefore, the length of the window used to divide a time series must be chosen such that it captures the transient frequencies of interest. If one can estimate the length (or duration) of each transient within the signal, then the window length to be used should correspond to the approximate length of the transient itself. This is attributed to the fact that windows of the same length as, or slightly shorter than, the transients fully encompass these without much interference from the stationary data, which results in strong Fourier modes within the transient frequencies. These transient-induced Fourier modes significantly contribute to the tails of the distributions in the corresponding frequency bins and are more easily captured by higher-order spectral moments. Conversely, the higher-order spectral moments decrease significantly as the window width is increased beyond the length of the transients because the windows that contain the transients become dominated by the stationary data. However, the length of each transient is rarely known *a priori*, and thus the ideal window length to be used may be initially unknown in certain applications, including the present one. One solution is therefore to compute the windowed Fourier transform using different window lengths to determine the optimum value (keeping in mind that relatively large windows will systematically result in Gaussian higher-order spectral moments). However, if one knows the approximate location of the transients in the frequency domain space beforehand, one can identify a few window lengths *a priori* that may work well. In the case where the frequency location of the transients is unknown, one may use the Kurtogram algorithm, proposed by Antoni (2007). This algorithm efficiently conducts a preliminary analysis and sweeps through the signal of interest using multiple window lengths to determine the optimal window to be used for further analysis. The results of this method are analogous to performing successive zooms in wavenumber space. A similar method

in which window lengths were increased in successive steps to improve the frequency resolution was initially used herein to find the approximate locations of the intermittent activity. Then, the most relevant window length to be used for analysis was determined by first establishing the wavenumber range to be studied using higher order spectral moments (e.g. $\kappa_{1low} \leq \kappa_1 \leq \kappa_{1high}$). The lower bound ($\kappa_{1low}$), which dictated the window size, was selected as a function of the range of scales of interest, whereas κ_{1high} was always equal to $1/\eta$ in the present work. κ_{1low} was then converted to a frequency (using Taylor's hypothesis: $f_{low} = \langle U \rangle \kappa_{1low}/(2\pi)$), which resulted in the lowest frequency needing to be spanned by the window. The minimum window length (in terms of samples, N_{min}) is given by $N_{min} = f_{samp}/f_{low}$, where f_{samp} is the sampling frequency.

2.2.3 Algorithm testing and validation

Before situating and quantifying internal intermittency in turbulent velocity and scalar fields using the approach outlined in §2.2.1, benchmarking of the algorithm was undertaken to ensure that the algorithm can properly detect transients.

As a first test, a time series of Gaussian white noise was generated using MATLAB and its spectral skewness and kurtosis were evaluated using the procedure described in §2.2.1 to ensure that the algorithm did not falsely detect transients. The artificial signal consisted of 244 blocks of 4096 data points sampled at a frequency of 10 kHz. As recommended in §2.2.2, several window lengths were evaluated to ensure that the results were consistent and not systematically forced to their Gaussian values by the Central Limit Theorem. Figure 2.3 confirms that the algorithm returns the values of $\Gamma(5/2)$ (≈ 1.33) and 2 for the spectral skewness and kurtosis, respectively, of a stationary, Gaussian signal. It is therefore clear that the algorithm does not detect significant deviations from Gaussianity, regardless of the window length, such

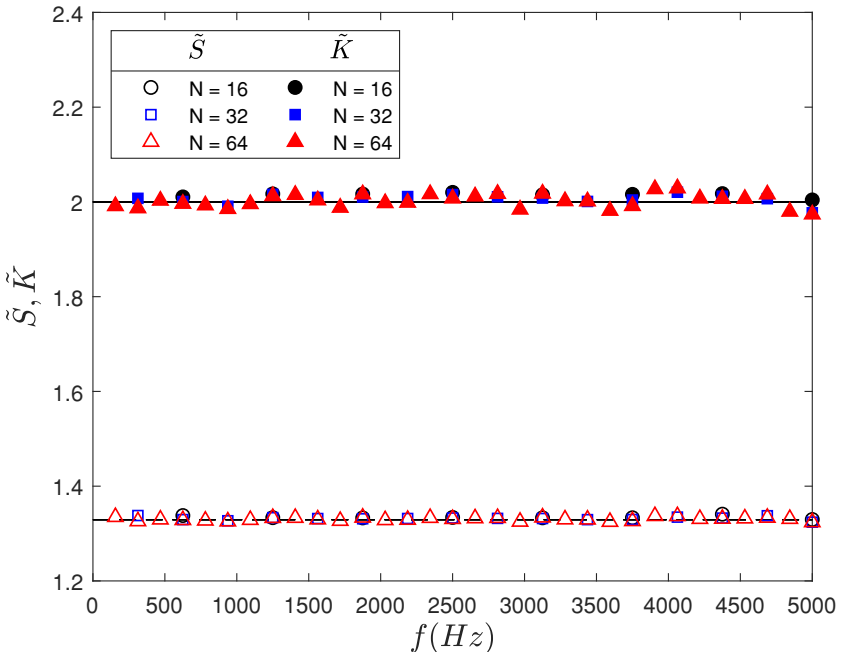

Figure 2.3: Spectral skewness (open symbols) and kurtosis (closed symbols) of Gaussian white noise evaluated using window lengths of 16 (∘,•), 32 (□,■), 64 (△,▲) samples. The lines represent the expected values of spectral skewness (dashed) and spectral kurtosis (solid) for stationary, Gaussian signals.

that any future observed deviations from Gaussianity will have originated from the intermittent behaviour of the turbulent signal.

To further test the algorithm's ability to detect transients and intermittent behaviour, another synthetic signal was constructed. It consisted of Gaussian white noise to which 11 short-lived transients of the form:

$$x_{trans}(t) = A\cos(2\pi ft)e^{(\lambda(t-\tau)^2)} \tag{2.18}$$

were superimposed, where f (the frequency of the transient) was varied from 990 Hz to 1010 Hz and a unique temporal offset (τ) was randomly attributed to each transient. The discretised signal had a sampling frequency of 10 kHz and the magnitude

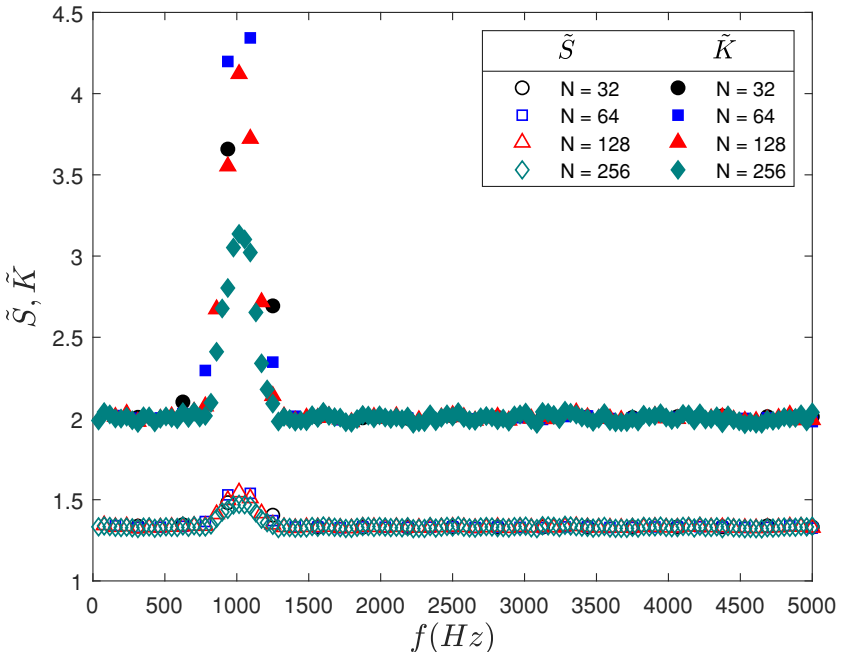

Figure 2.4: Spectral skewness (open symbols) and kurtosis (closed symbols) of Gaussian white noise with added transients evaluated using window lengths of 32 (∘,•), 64 (□,■), 128 (△,▲), 256 (◇,◆) samples.

of each transient was within 99.9% of its maximum amplitude (A) for 0.0074 seconds. Note that the purpose of this synthetic signal was not to emulate turbulence, as the physics underlying the internal intermittency of turbulent flows are much more complicated. Rather, the synthetic signal is used to benchmark the ability of the higher-order spectral moments tools to detect short, intermittent behaviour. The higher-order spectral moments of this signal are depicted in figure 2.4, in which one can observe a clear deviation from Gaussianity being detected by the algorithm around 1.0 kHz, which corresponds to the frequency of the added transients. Note that the skewness captures and locates the transients well, even though rare events in a given process may occur symmetrically (i.e. evenly in both tails of the distribution). The reason the spectral skewness is capable of detecting transients is that

the tails of the distribution become combined when taking the magnitude of the Fourier modes. This concentrates the rare events to a single tail, which skews the distribution. Moreover, it is worth noting that the spectral kurtosis appears to be more sensitive to transients than the spectral skewness. This results from the higher statistical order of the spectral kurtosis. Figure 2.4 also clearly demonstrates that the magnitudes of the deviations from Gaussian behaviour decrease with increasing window length, further reinforcing the notion that higher order spectral moments are dependent on the window length (N). In this particular example, the effects of the window length are easily explained by comparing the length of the transients (n_{trans}) to N. The number of sample points contained within each transient is equal to $n_{trans} = f_s \times t_{trans}$, where f_s is the sampling frequency and t_{trans} is the duration of the transient. As previously mentioned, the transients in this example are approximately 0.0074 seconds long, yielding approximately 74 data points within each transient. Therefore, given the discussion in §2.2.2, one could anticipate that a window length of $N = 74$, or slightly shorter, would maximize the higher-order spectral moments. The results presented in figure 2.4 support this argument, as the peak value of both spectral moments decrease as the length of the windows exceed the length of the transients in the signal. Moreover, as the window length is shortened significantly below the length of the transients, the peak values of the higher-order spectral moments decrease as well. Nevertheless, the deviations from Gaussian behaviour are accurately situated and quantified in the frequency domain regardless of the window length, thus showing that the algorithm constructed in §2.2.1 is capable of capturing rare, intermittent events in an otherwise Gaussian time series.

CHAPTER 3
Experimental data and apparatus

This chapter presents a detailed discussion of the experimental data analysed and apparatus used to acquire turbulent velocity and passive scalar fields. Two different types of flows are analysed herein: (i) grid-generated, wind tunnel turbulence and (ii) turbulent channel flow. The first data set consists of velocity and passive scalar field measurements obtained by L. Mydlarski at Cornell University in 1996 and published in Mydlarski and Warhaft (1998). The second set of data consists of velocity measurements acquired by the author in the turbulent channel of the Aerodynamics Laboratory at McGill University.[1] This chapter begins with a brief overview of the grid-turbulence data. Note that the wind-tunnel facility is only briefly described as detailed discussions are provided in Mydlarski and Warhaft (1996) and Mydlarski and Warhaft (1998). This is followed by a description of the channel apparatus and flow conditions. Finally, the instrumentation used to makes the measurements is described, including a discussion of the filtering and data acquisition apparatus.

3.1 Passive and active grid turbulence data

The wind-tunnel data analysed herein was first obtained as part of the work of Mydlarski and Warhaft (1998) from experiments conducted in two different wind tunnels in the Sibley School of Mechanical and Aerospace Engineering at Cornell

[1] Due to the COVID-19 pandemic and the resulting closure of the University, the initial part of this research was undertaken using data previously acquired by the author's supervisor.

University. The first tunnel was vertically oriented and had a test section that is 40.65×40.65 cm^2 in cross-section and 4.5 m long, and the test section of the second one was horizontally oriented and had a 91.44×91.44 cm^2 cross-section and is 9.1 m in length. The flow parameters for the cases analysed herein are presented in Table 3–1. For the $R_\lambda = 35$ and $R_\lambda = 86$ cases, the turbulence was generated by means of passive grids with 2.54 cm and 10.19 cm mesh lengths, respectively. The turbulent flow fields in all other cases were generated using active grids based on the design of Makita (1991). The active grids contain bars driven by stepper motors that independently actuate rows of agitator wings to create approximately homogeneous, isotropic turbulence (Mydlarski & Warhaft, 1996; Mydlarski, 2017). Active grids were used to achieve a maximum Taylor microscale Reynolds number of $R_\lambda = 731$. A uniform, mean, cross-stream temperature gradient was generated using differentially heated metallic ribbons at the entrance to the wind tunnels' settling chambers. The action of the turbulent velocity field on this mean temperature gradient resulted in a turbulent passive scalar (temperature) field.

Simultaneous two-component (u,v) velocity and temperature measurements were made in all but two cases. Only longitudinal velocity measurements were made for the $R_\lambda = 671$ case, and separate longitudinal velocity and temperature measurements were made at $R_\lambda = 731$. In these two ($R_\lambda = 671$ and $R_\lambda = 731$) cases, the velocity measurements were obtained using a single-normal tungsten hot-wire sensor, whereas an X-wire sensor was used for all the other cases. In all cases, hot-wire overheat ratios of 1.8 were employed using Dantec 55M01 constant temperature anemometers. The temperature measurements were made using a cold-wire thermometer sensor placed in a plane parallel to, but 0.5 mm away from, the X-wire sensor. The data were low- and high-pass filtered, and then digitized using an A/D card. Further information

Tunnel	Horiz.	Vert.	Horiz.	Horiz.	Vert.	Vert.	Horiz.	Vert.	Horiz.	Horiz.	Horiz.
Grid	Passive	Active	Passive	Active	Active	Active	Active	Active	Active	Active	Active
Mesh (cm)	2.54	5.08	10.2	11.4	5.08	5.08	11.4	5.08	11.4	11.4	11.4
$\langle U \rangle$ (m s^{-1})	6.3	3.3	6.2	3.3	3.6	12.2	3.3	11.4	7	7.3	6.9
x/M	70	68	70	62	68	68	62	68	62	35	31
β ($^\circ$C m^{-1})	5.9	4.8	7.4	2.5	3.3	5.2	2.7	3.6	3.6	n/a	5.1
ν ($\times 10^{-6}$ m^2 s^{-1})	15.9	16.0	15.8	15.5	16.0	16.0	16.0	16.0	16.0	15.5	15.0
$\langle u^2 \rangle$ (m^2 s^{-2})	0.0134	0.0156	0.0208	0.029	0.0629	0.311	0.0911	1.04	0.583	1.42	1.44
$\langle u^2 \rangle^{1/2} / \langle U \rangle$ (%)	1.8	3.8	2.1	5.2	7.0	4.9	9.1	8.9	10.9	16.4	17.4
$\langle \epsilon \rangle$ (m^2 s^{-3})	0.135	0.0314	0.0559	0.0418	0.118	2.33	0.0833	6.13	0.94	4.48	3.88
$L (= 0.9 \langle u^2 \rangle^{3/2} / \langle \epsilon \rangle)$ (m)	0.010	0.056	0.048	0.11	0.12	0.067	0.3	0.16	0.43	0.34	0.4
$R_\lambda (= \langle u^2 \rangle \{15/(\nu \langle \epsilon \rangle)\}^{1/2})$	35	85	86	140	177	197	306	407	582	671	731
$R_L (= \langle u^2 \rangle^{1/2} l/\nu)$	75	440	441	1200	1900	2300	5600	9900	20300	26000	32100
$\eta (= (\nu^3/\langle \epsilon \rangle)^{1/4})$ (mm)	0.42	0.6	0.52	0.55	0.43	0.21	0.47	0.16	0.26	0.17	0.17
$\langle \epsilon_\theta \rangle$ ($^\circ$C^{2}s^{-1})	0.0284	0.0595	0.140	0.128	0.0665	0.197	0.360	0.215	0.789	n/a	1.70
$\langle \theta^2 \rangle$ ($^\circ$C^2)	0.0081	0.062	0.143	0.176	0.083	0.055	0.8	0.08	1.07	n/a	2.05
$l_\theta (= \langle \theta^2 \rangle^{1/2}) / \beta$ (m)	0.015	0.052	0.051	0.17	0.087	0.0451	0.33	0.079	0.29	n/a	0.28
$f_\eta (= \langle U \rangle / (2\pi\eta))$ (kHz)	2.4	0.88	1.9	0.95	1.3	9.4	1.1	11.3	4.3	6.8	6.5

Table 3–1: Wind tunnel flow parameters. These eleven cases were used to calculate the higher-order spectral moments. The velocity and scalar dissipation rates were determined using $\langle \epsilon \rangle = 15\nu \int_0^\infty \kappa_1^2 F_{11}(\kappa_1) d\kappa_1$ and $\langle \epsilon_\theta \rangle = 3\gamma \int_0^\infty \kappa_1^2 F_\theta(\kappa_1) d\kappa_1$. The Prandtl number (Pr) was 0.7.

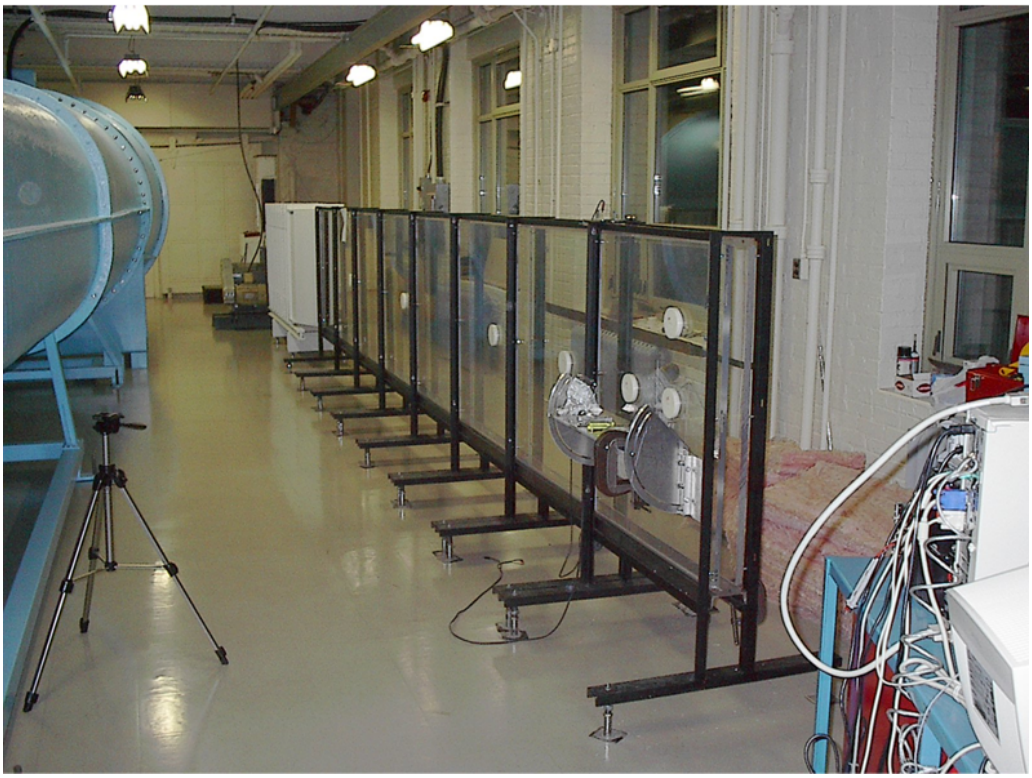

Figure 3.1: Picture of the channel flow facility located in the Aerodynamics Laboratory at McGill University.

on the equipment, as well as detailed descriptions of the wind tunnels and the active grids, are given in Mydlarski and Warhaft (1996) and Mydlarski and Warhaft (1998).

3.2 Channel flow data

This section begins with an overview of the channel facility used to make wall-bounded flow measurements. The flow parameters for the test cases presented herein then follow. Finally, the instrumentation and data acquisition equipment is presented, along with the sources of error that are to be expected with the equipment.

3.2.1 Channel facility

The channel used to make wall-bounded flow measurements is shown in figure 3.1. The apparatus consists of a blower, a flow conditioning section, and a long test

section in which the flow becomes fully developed.

The blower is a Hudson Buffalo ACL (size 330 CL2) model and is connected to a 7.5 hp motor controlled by an ABB ACS 600 controller. The blower intake contains a filter box capable of filtering particles greater than 3 μm. The assembly is supported by soft rubber footpads to reduce vibrations and is connected to the flow conditioning section via rubber coupling joints to avoid transmitting vibrations to the rest of the apparatus.

The flow conditioner is composed of three sections: a diffuser, a settling chamber, and a contraction. The diffuser's purpose is to reduce the speed of the flow before it enters the settling chamber. This causes the flows to remain in the settling chamber for a longer period of time. The diffuser has a 45° angle, which would normally cause flow separation due to the adverse pressure gradient resulting from the expansion (Mehta & Bradshaw, 1979). However, flow separation is prevented by the presence of four screens that cause pressure drops to balance the pressure increase that arises from the expansion. The settling chamber has the same height as the channel and consists of a rectangular, constant-cross-sectional area section. Its main purpose is to further homogenise the flow. This is achieved using a carefully positioned 76 mm long honeycomb section with 6.35 mm wide hexagonal cells and screens with 1 mm meshes. Given that the settling chamber has the same height as the channel, the contraction that connects the settling chamber to the channel is two-dimensional. A contraction ratio of 8:1 is used and the shape of the contraction is based on a fifth order polynomial (see Lavertu and Mydlarski (2005) for more information on the contraction design).

The flow exiting the contraction and entering the channel is uniform and has a turbulence intensity of 0.25% (Lavertu & Mydlarski, 2005). The channel height

(b) is 1.1 m and its width ($2h$) is 0.06 m (see Figure 1.3). Given the high-aspect-ratio ($b \gg h$), the flow is statistically two-dimensional far enough from the top and bottom walls. The total length of the channel test section is 8 m, and its walls are made of plexiglass sheets. The region of the test section in which measurements were made extends from 7.0 m to 7.67 m away from the test section inlet. A custom machined port located 7.33 m away from the channel entrance and at the centre of the vertical wall (i.e. at $b/2$) was used to make the measurements presented herein. To ensure that the flow becomes fully developed before reaching the test section, 3.2 mm diameter rods that trip the boundary layer were placed 60 mm from the channel entrance and 3 mm from each vertical wall.

3.2.2 Flow conditions

The turbulent channel flow results presented in chapter 4 were obtained by making velocity at a downstream location of $x/h = 244$ and at blower rotational speed of 692 rpm. The resulting friction velocity (u_τ) was found to be 0.43 m/s.

The (absolute and normalized) wall-normal measurement locations, as well as the flow conditions are given for all cases in table 3–2. Longitudinal hot-wire anemometry (u) measurements were made in all cases, achieving Taylor microscale Reynolds numbers in the range $86 \leq R_\lambda \leq 159$.

3.3 Instrumentation

This section discusses the instrumentation, beginning with an overview of hot-wire anemometry, followed by an presentation of the calibration procedure. The data acquisition hardware and software is then presented. Note that the sources of error and corresponding uncertainties that arise with hot wire-anemometry are discussed in Appendix B.

y (mm)	0.15	0.2	0.3	1	5	15	20	25	30
y/h	0.0050	0.0067	0.010	0.033	0.17	0.5	0.67	0.083	1.0
y^+	4.4	5.8	8.7	29.0	145	436	581	726	872
$\langle U \rangle$ (m s^{-1})	5.42	5.47	5.47	5.87	7.01	8.19	8.55	8.76	8.77
$\langle u^2 \rangle$ (m^2 s^{-2})	0.794	0.785	0.726	0.569	0.422	0.230	0.162	0.112	0.0948
$\langle u^2 \rangle^{1/2} / \langle U \rangle$ (%)	16.5	16.2	15.6	12.8	9.3	5.9	4.7	3.8	3.5
$\langle \epsilon \rangle$ (m^2 s^{-3})	24.7	24.3	23.7	18.8	8.02	2.76	1.82	1.32	1.16
L (m)	0.012	0.016	0.016	0.019	0.029	0.035	0.040	0.029	0.031
$R_\lambda (= \langle u^2 \rangle \{15/(\nu \langle \epsilon \rangle)\}^{1/2})$	159	159	149	131	149	138	120	97	88
$R_L (= \langle u^2 \rangle^{1/2} l/\nu)$	1520	1520	1330	1030	1330	1150	859	565	463
$\eta (= (\nu^3/\langle \epsilon \rangle)^{1/4})$ (mm)	0.11	0.11	0.11	0.12	0.14	0.19	0.21	0.23	0.23
$f_\eta (= \langle U \rangle / (2\pi\eta))$ (kHz)	8.0	8.0	7.9	8.1	7.8	7.0	6.5	6.2	6.0

Table 3–2: Channel flow parameters. These nine cases were used to calculate the higher-order spectral moments. The velocity dissipation rates were determined using $\langle \epsilon \rangle = 15\nu \int_0^\infty \kappa_1^2 F_{11}(\kappa_1) d\kappa_1$ and the integral length scales were determined using $L = \int_0^\infty \langle u(x+r)u(x) \rangle / \langle u^2 \rangle dr$. The kinematic viscosity (ν) was 15×10^{-6} m^2/s and the friction Reynolds number was $R_\tau = u_\tau h/\nu = 860$ where $u_\tau = 0.43$ m/s is the friction velocity and $h = 0.030$ m is the channel half-width.

3.3.1 Hot-wire anemometry

Hot-wire anemometers are commonly used in fluid mechanics research to measure fluid velocity and in turbulent flows. The technique relies upon on convective heat transfer from a very fine, heated wire or film to the surrounding fluid. Hot-wire anemometers can be operated in the constant-current or constant-temperature mode, though the latter is much more common for velocity measurements. (See Bruun (1995) for a comparison of these two operating modes.)

Proper operation of a hot-wire probe requires appropriately setting the overheat ratio, which is ratio of the wire when heated to its resistance at the ambient temperature (R_w/R_a). An overheat ratio greater than one increases the operating temperature of the wire, which makes it more sensitive to velocity changes. However, if the operating temperature is too high, wire may oxidise. To avoid oxidization and obtain a reasonable sensitivity, a value of R_w/R_a = 1.8 is recommended by Bruun (1995) for velocity measurements in air.

For this work, a single-normal, TSI-1218 standard boundary layer probe was used to measure the velocity of the flow of air in the high aspect-ratio channel. A 5 μm tungsten wire was soldered to the probe, after which the newly-made hot-wire was aged by operating it at an overheat ratio of 1.8 for 24 hours. The aging process is required to allow the the properties of the hot-wire materials (and thus, its resistance) to reach steady-state before it is used to make measurements.

A DISA 55M01 constant temperature anemometer was used in these repetitive measurements. The probe support was mounted on a 0.02 inch/turn Velmex BiSlide to which a single shaft stepper motor was attached. Accurate positioning and translation of the probe was possible via the use of a VXM stepping motor controller, which enabled step-by-step rotation of the stepper motor.

The TSI-1218 boundary layer probe is equipped with a protective pin that creates a minimum separation of 0.13 mm between the wire and the wall, when the pin is in contact with the wall. Accurate initial positioning of the probe was therefore achieved by gradually moving the probe closer to the wall (using the traversing mechanism discussed above), until the protective was seen to touch the wall. The position of the probe was then known to be $y = 0.13$ mm and any subsequent position of the probe could be calculated from the displacement commands sent via the VXM stepping motor controller.

3.3.2 Calibration of hot-wire probes

The heat transfer from the heated wire to the fluid depends on the velocity of the fluid. Therefore, it is possible to correlate the voltage output of the anemometer to the velocity of the flow. For a single-normal wire, this correlation takes the following form:

$$E^2 = A + BU^n, \tag{3.1}$$

which is often referred to as King's Law. In this equation, E is the output voltage of the anemometer, U is the velocity of the flow, and A, B, and n are calibration constants.

The hot-wire probe is calibrated by placing it in a steady, laminar flow of known velocity created using a TSI 1128 Air Velocity Calibrator. The calibrator consists of a jet with a top-hat velocity profile at its exit. A pressure transducer is connected upstream of the jet exit. By measuring the the difference between this pressure and the ambient pressure (which is the pressure at the jet exit), it is possible to calculate the velocity of the fluid of the jet. During the calibration, the velocity of the jet is

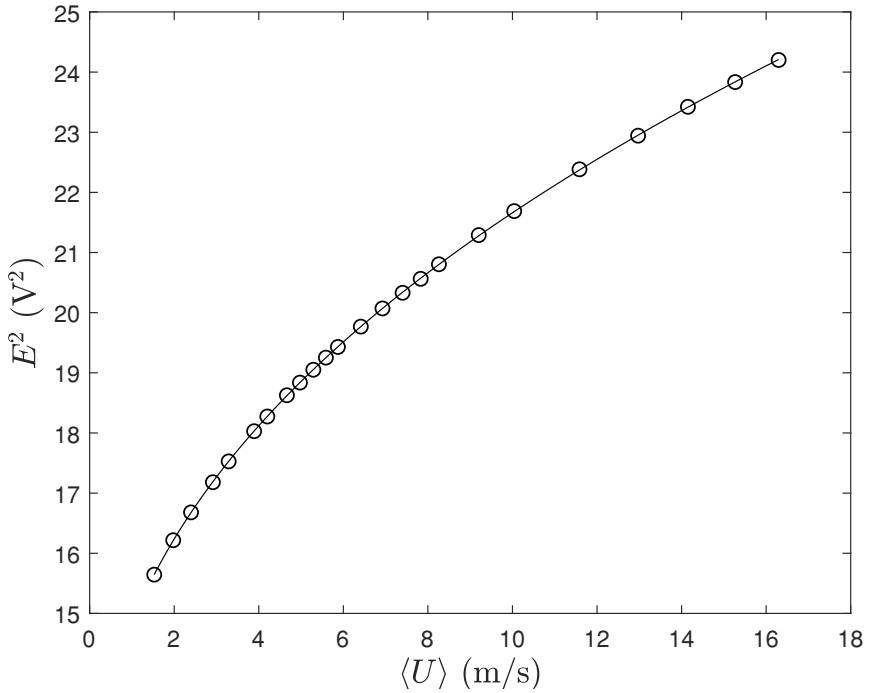

Figure 3.2: Calibration data (∘) for a TSI-1218 standard boundary layer probe with King's Law fit (solid line).

changed progressively. The voltage output of the anemometer (E) is recorded for each jet velocity to create a calibration curve.

A sample calibration curve obtained using the TSI-1218 standard boundary layer probe connected to a DISA 55M01 anemometer is shown in figure 3.2. From the data, the calibrations constants of equation 3.1 are determined to be A = 10.89, B = 3.959, and n = 0.4348. Note that the various sources of error that arise from the calibration of hot-wire probes and the resulting uncertainties are discussed in Appendix B.

3.3.3 Data acquisition

The output voltage of the DISA 55M01 anemometer was low- and high-pass filtered using a Krohn-Hite Model 3382 filter. A National Instruments model BNC-2110 analogue-to-digital (A/D) board was used in these experiments to record the data to a computer. This A/D board is a 16-bit instrument which separates the range of operating voltages into 2^{16} discrete steps. Low-pass filtering was necessary to remove high frequency electronic noise. High-pass filtering at (0.01 Hz) was also used to remove the mean component of the signal, and very low frequency, non-turbulent velocity fluctuations. The filtered signal that remained therefore corresponded to the deviations from the mean velocity. To amplify these fluctuations and maximize the 16-bit resolution ($\pm$5 V range) of the A/D board, a gain of 5 dB was set at the output of the low-pass filtered channel and a gain of 20 dB was set at the output of the high-pass filtered channel.

At each probe location, the low-pass frequency was determined using a spectrum analyzer, to estimate the frequency at which the signal becomes lower than the noise floor. The low-pass frequency was set to this value using the Krohn-Hite Model 3382 filter. Note that the average of the low-pass filtered signal was measured at each probe location to determine the average voltage output of the anemometer before removing the mean by way of high-pass filtering. This mean voltage measurement was then used to find the mean velocity of the flow.

The data recorded by the A/D board can be represented mathematically as:

$$E_m = G(E_{anem} - E_{mean}), \tag{3.2}$$

where E_m is the filtered and amplified voltage recorded by the A/D board, G is the total gain, E_{mean} is the mean voltage, and E_{anem} is the unamplified voltage put

out by the DISA 55M01 anemometer. To calculate the velocity from the voltages recorded by the A/D board, amplification and filtering must be taken into account before using equation 3.1. Rearranging equation 3.2 and substituting it into equation 3.1, the velocity corresponding to each data point can be calculated using (Bruun, 1995):

$$U = \left(\frac{\left(\frac{1}{G}E_m + E_{mean}\right)^2 - A}{B} \right)^{1/n}, \tag{3.3}$$

where U is the instantaneous velocity. Note that, for this experiment, the total gain (G) corresponds to the combination of the gain applied at the low-pass filter (5 dB) output and the high-pass filter output (20 dB): G = 5 dB +20 dB = 25 dB.

CHAPTER 4
Results and discussion

The higher-order spectral moments estimation method outlined and verified in chapter 2 is used hereafter to quantify the evolution of intermittent behaviour in turbulent flows across wavenumber space. This section begins with a presentation of the quantification and comparison of the internal intermittency of velocity and passive scalar fields obtained in grid-generated, wind-tunnel turbulence. This is followed by an investigation of the detection of coherent structures in the near-wall region of a turbulent channel flow by way of higher order spectral moments.

4.1 Quantification of internal intermittency by way of higher-order spectral moments

This section presents an investigation of the internal intermittency of turbulent velocity fields by way of higher-order spectral moments. Of particular interest is the Reynolds number dependence of the higher-order spectral moments of turbulent velocity and scalar fields, as well as a comparison of the higher-order spectral moments of the same fields.

4.1.1 Higher-order spectral moments of turbulent velocity fields

Higher-order spectral moments of turbulent time series are presented in figures 4.1 and 4.2, which respectively plot the spectral skewness and spectral kurtosis of a turbulent velocity field at R_λ = 582 as a function of normalised wavenumber ($\kappa_1\eta$). Normalised, one-dimensional power spectra ($F_{11}(\kappa_1\eta)$) are also plotted in these figures to better identify the various ranges of the flow (e.g. the inertial subrange).

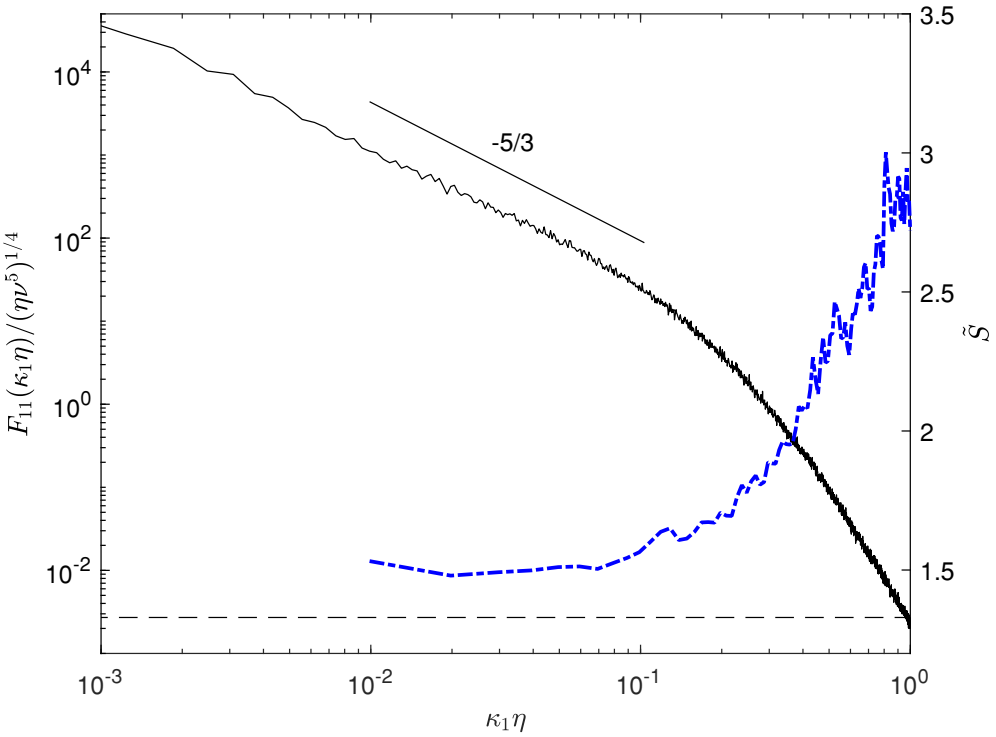

Figure 4.1: Longitudinal (u) velocity spectrum (solid black line) and spectral skewness (dot-dashed blue line) at R_λ = 582. Results are obtained using a window length 625η.

Note that these results were obtained using STFT windows of length $N = 625\eta$. Although shorter windows would have maximised the higher-order spectral moments, longer windows include a larger range of frequencies, which is preferable at the initial stages of the analysis, given that they allow low-frequency deviations from Gaussianity to also be captured. Results obtained using shorter windows that highlight the intermittency at higher frequencies are presented in subsequent sections.

It is worthwhile noting that some insight could have been gained from calculating the higher-order moments of differences in turbulent quantities (e.g. the kurtosis of velocity increments, $K_{\Delta u}$, ($\Delta u = [u(x + r) - u(x)]$)), as those are the real-space analogues of the spectral moments of equivalent statistical order. However, as noted

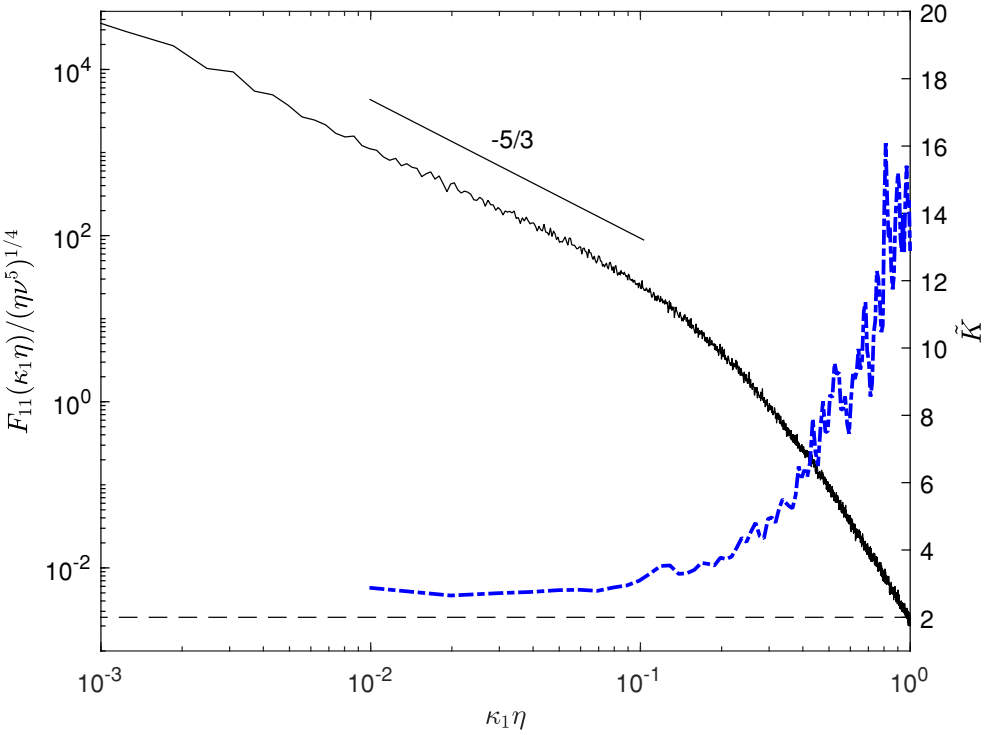

Figure 4.2: Longitudinal (u) velocity spectrum (solid black line) and spectral kurtosis (dot-dashed blue line) at $R_\lambda = 582$. Results are obtained using a window length 625η.

in §1.2, an important reason for undertaking the present analysis in the spectral domain is that structure functions (e.g. $\Delta u(r)$) include contributions from *all* scales less than or equal to the scale r (see, for example, Meyer et al. (2018)), whereas spectra quantify the contribution *only* at a specific scale ($\kappa_1 \sim 1/r$).

The first important observation to be made regarding figures 4.1 and 4.2 is that both higher-order spectral moments asymptotically tend to their Gaussian values ($\tilde{S} = \Gamma(5/2)$ and $\tilde{K} = 2$) at large scales (low wavenumbers), thus confirming that little intermittency is present at the largest scales of the turbulence. Conversely, at high wavenumbers, one observes a sharp increase in both the spectral skewness and kurtosis, thus highlighting the highly intermittent behaviour of the turbulent

velocity field at dissipative scales. Note that these observations are consistent with figure 6 of Brun and Pumir (2001) and figure 1(a) of Chevillard et al. (2005), who observed a plateau at large scales and increased intermittent activity in the dissipation range using fourth-order spectral moments applied to time series of velocity fields from numerical and experimental data, respectively. Chevillard et al. (2005) also calculated the fourth-order spectral moment of an intermittent synthetic signal, as a proxy for turbulence at high Reynolds number (with no dissipation range), which yielded a similar plateau. They found that the magnitude of the plateau evolved as a power-law of the width of the windowing function (arguing that longer windows were associated with larger scales and therefore lower values of the fourth-order spectral moments). However, the analysis presented in §2.2.1 demonstrated that longer window lengths are associated with lower values of the higher-order spectral moments due to consequences of the Central Limit Theorem.

These preliminary observations clearly demonstrate that both higher-order spectral moments studied herein are able to detect deviations from Gaussianity and thus internal intermittency. Moreover, the insight provided by the higher-order spectral moments compared to time-domain statistical moments is also readily demonstrated. The calculation of higher-order moments in short spectral bands allows (i) deviations from Gaussian behaviour to be located in wavenumber space, and (ii) an evaluation of the relative magnitude of the deviations from Gaussianity at each scale. The deviation from Gaussianity extends to the high-wavenumber end of the inertial subrange. This will be further discussed when short-window results are introduced, as these provide an even better depiction of inertial-subrange intermittency. These features of higher-order spectral moments will be used to further study the internal intermittency of turbulent velocity and passive scalar fields in the following sub-sections.

4.1.2 Reynolds number dependence of higher-order spectral moments

Figure 4.3 depicts the evolution of the spectral skewness and kurtosis of the longitudinal velocity fluctuations (u), transverse velocity fluctuations (v), and scalar fluctuation (θ) in grid generated turbulence at five different Reynolds numbers in the range $35 \leq R_\lambda \leq 582$. Note that these results were generated using a relatively short window length of $N = 150\eta$, thereby highlighting transient behaviour at the smaller-scale end of the inertial subrange and in the dissipation range. The results depict a very clear dependence on Reynolds number, even at $R_\lambda < 100$ which was previously observed to be the threshold for the hydrodynamic (inertial-range) intermittency exponent (μ) to depart from zero (Mydlarski & Warhaft, 1996).[1] A significant increase in non-Gaussian behaviour is exhibited by all spectral moments as the Reynolds number is increased. Note that this increase in magnitude of the spectral moments occurs at all scales covered by the chosen window length, and applies to all turbulent fields under study (i.e. u, v, and θ). Moreover, note that the scale at which a strong and rapid departure from Gaussianity is observed shifts towards larger scales as the Reynolds number increased.

One can further explore the Reynolds number dependence of internal intermittency by investigating the evolution of the magnitude of the higher-order spectral moments evaluated at a particular length scale. A length scale of interest is the wavenumber at which the dissipations of turbulent kinetic energy and turbulent scalar variance spectra peak, which is observed to occur around $\kappa_1\eta = 0.2$ for the

[1] However, Mydlarski and Warhaft (1998) observed the scalar field intermittency exponent (μ_θ) to be non-zero at even the lowest of Reynolds/Péclet numbers.

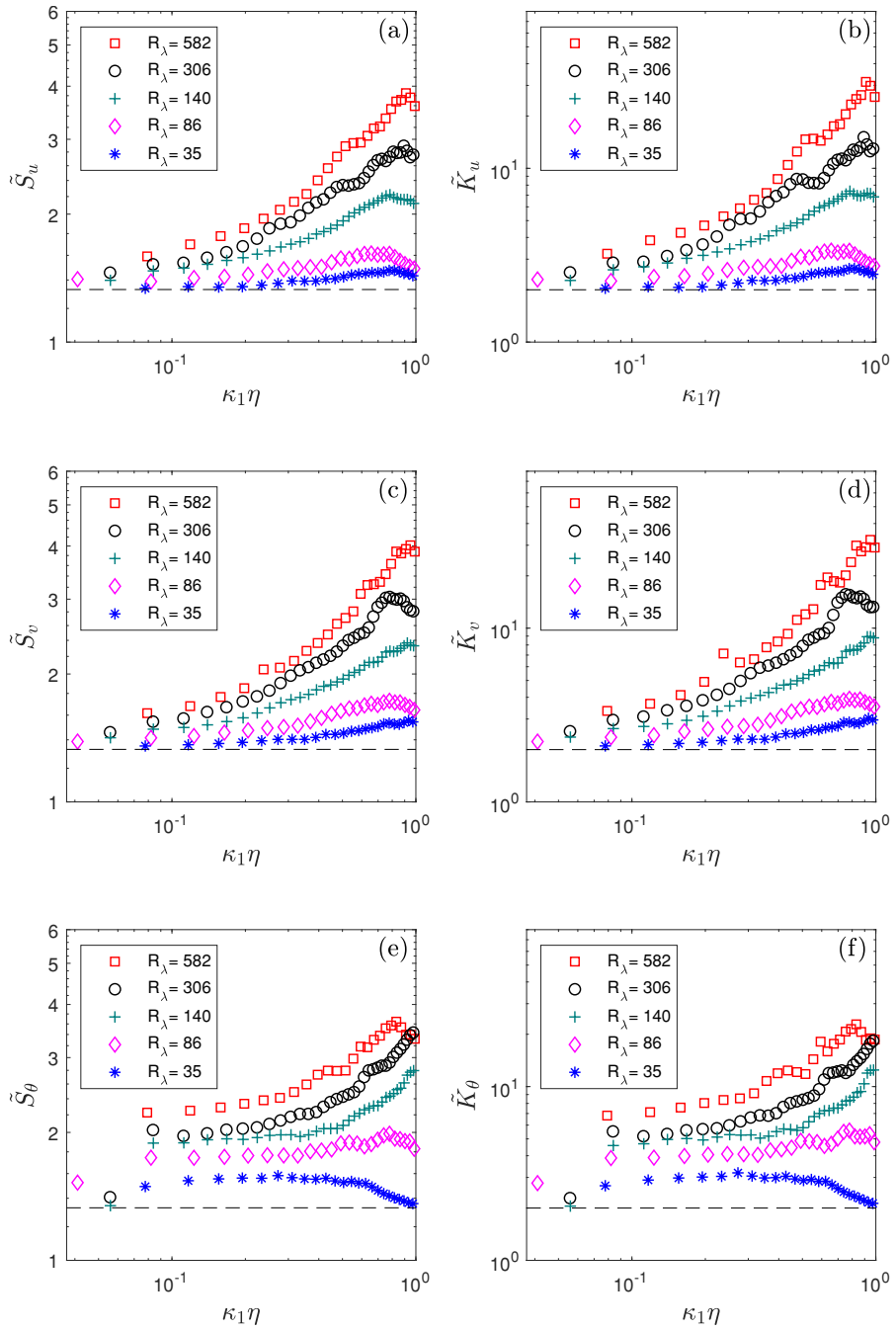

Figure 4.3: Spectral skewness (a, c, e) and kurtosis (b, d, f) of the longitudinal velocity fluctuations u (a, b), the transverse velocity fluctuations v (c, d), and the scalar (temperature) fluctuations θ (e, f) at R_λ = 35 (∗), R_λ = 86 (◇), R_λ = 140 (+), R_λ = 306 (∘), and R_λ = 582 (□). Results are obtained using a window length $N = 150\eta$.

velocity and scalar fields, though the exact location of this peak is Reynolds number dependent (Tennekes & Lumley, 1972; Mydlarski & Warhaft, 1996, 1998). The value of the spectral skewness and kurtosis at a normalised wavenumber of $\kappa_1\eta = 0.2$ is plotted in figure 4.4 as a function of R_λ over the range $35 \leq R_\lambda \leq 731$. Note that the higher-order spectral moments shown in figure 4.4 were obtained using the same window length as that used in figure 4.3 ($N = 150\eta$). Though some scatter is observed, the plots confirm the increase in both the spectral skewness and spectral kurtosis (and therefore in internal intermittency) at a fixed normalised wavenumber as R_λ is increased. Moreover, considering each higher-order spectral moment individually, note that the power law fits are consistent for the longitudinal and transverse velocity and passive scalar fields, with $\tilde{S}(\kappa_1\eta = 0.2)$ approximately increasing as $R_\lambda^{0.1}$ and $\tilde{K}(\kappa_1\eta = 0.2)$ approximately increasing as $R_\lambda^{0.3}$ for the spectral kurtosis. The evolution of the spectral skewness and kurtosis is further explored in figure 4.5, in which the Reynolds number dependence of both spectral moments evaluated at $\kappa_1\eta = 0.8$ is investigated. Note that the chosen length scale of $\kappa_1\eta = 0.8$ is believed to offer a good representation of the intermittent behaviour of the flow as the Kolmogorov length scale is approached ($\kappa_1\eta \to 1$), while staying sufficiently far away from the Kolmogorov length scale where errors due to lowpass filter roll-off and probe frequency resolution (especially with cold-wire thermometers) may occur (Kuo & Corrsin, 1971). As was the case at $\kappa_1\eta = 0.2$, the Reynolds number dependence of the spectral skewness and kurtosis at $\kappa_1\eta = 0.8$ is consistent with a power law increase, though a stronger dependence on Reynolds number is observed at this smaller length scale. These changes in power law exponents with $\kappa_1\eta$ highlight the wavenumber dependence of the evolution of the higher-order spectral moments with R_λ.

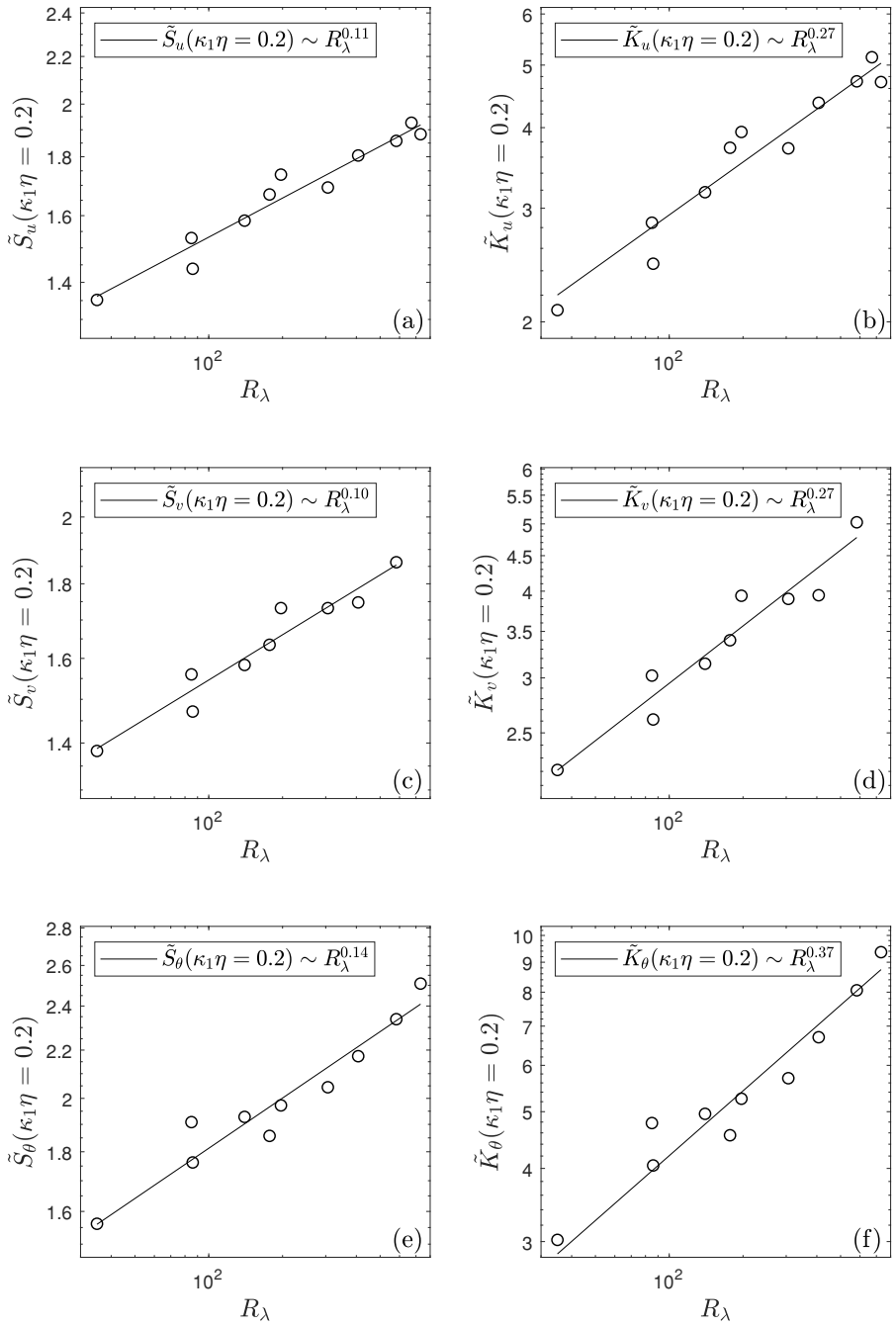

Figure 4.4: Reynolds number dependence of the spectral skewness (a, c, e) and kurtosis (b, d, f) of the longitudinal velocity fluctuations u (a, b), the transverse velocity fluctuations v (c, d), and the passive scalar (temperature) fluctuations θ (e, f) evaluated at $\kappa_1\eta$ = 0.2. The solid black lines represent the best fit power laws. Results are obtained using a window length N = 150η.

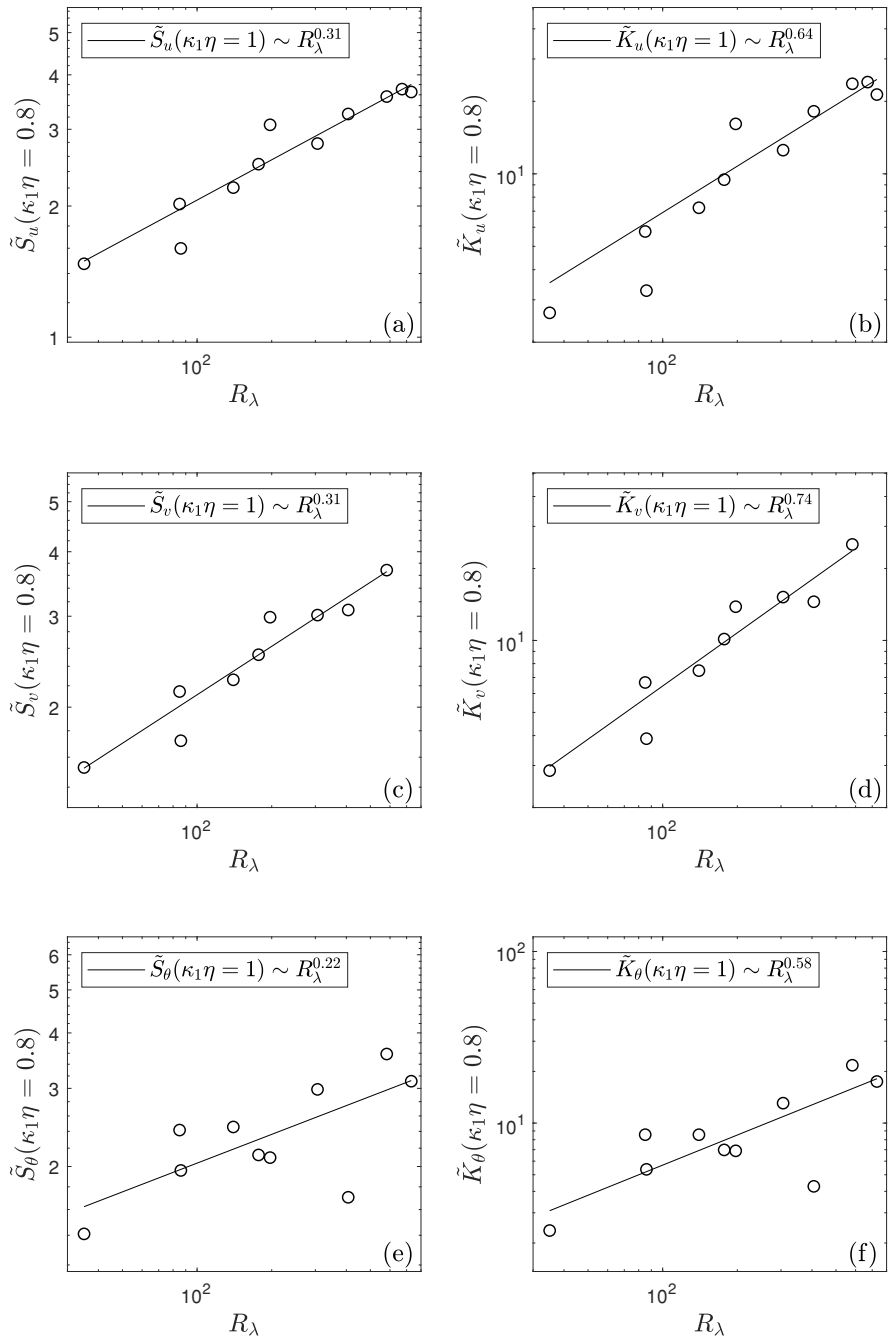

Figure 4.5: Reynolds number dependence of the spectral skewness (a, c, e) and kurtosis (b, d, f) of the longitudinal velocity fluctuations u (a, b), the transverse velocity fluctuations v (c, d), and the passive scalar (temperature) fluctuations θ (e, f) evaluated at $\kappa_1\eta$ = 0.8. The solid black lines represent the best fit power laws. Results are obtained using a window length N = 150η.

To place these results in the context of prior studies of internal intermittency, it is of benefit to compare the present work with prior investigations of the dependence of internal intermittency on Reynolds number, which was historically investigated using the kurtosis of derivatives of turbulence quantities (e.g. $K_{\partial u/\partial x}$, $K_{\partial \theta/\partial x}$) as measures of the degree of intermittency in turbulent flows (see Van Atta and Antonia (1980), Sreenivasan and Antonia (1997)). Studies have shown that $K_{\partial u/\partial x}$ and $K_{\partial \theta/\partial x}$ are strongly dependent on Reynolds number, with $K_{\partial u/\partial x}$ increasing as $\sim R_\lambda^{3/8}$ (Van Atta & Antonia, 1980), which is consistent with the observations of the spectral kurtosis evaluated at $\kappa_1\eta = 0.2$ (figure 4.4). As previously noted, the Reynolds number dependence of the spectral skewness and kurtosis was specifically evaluated at $\kappa_1\eta = 0.2$ because this normalized wavenumber ($\kappa_1\eta = 0.2$) approximately corresponds to that of the peak of the dissipation spectrum (Tennekes & Lumley, 1972). Given that dissipation spectra can also be interpreted as the spectra of the derivative, studying the higher-order spectral moments at $\kappa_1\eta = 0.2$ evaluates them at the wavenumber at which the derivative has its maximum contribution, thus explaining the agreement between the observed trends ($\sim R_\lambda^{0.3}$) and those obtained by examining the Reynolds number dependencies of $K_{\partial u/\partial x}$ and $K_{\partial \theta/\partial x}$ ($\sim R_\lambda^{3/8}$). However, it bears reiterating that the present results have demonstrated that the Reynolds number dependence of internal intermittency depends upon wavenumber, as demonstrated by the scale-by-scale analysis achieved by way of higher-order spectral moments.

In addition to the above results, another approach was also employed in an attempt to investigate any possible Reynolds number dependencies associated with the use of a window length of fixed multiples of η as the Reynolds number changes. To this end, the data was reanalysed using a window length (N) that evolved with Reynolds number in such a way the window length was equal to the separation that

corresponds to the mid-point of the inertial subrange for each flow. To determine the required window length for this approach, the methodology employed in Mydlarski and Warhaft (1996, 1998), who developed an approach for the calculation of conditional statistics of inertial-range velocity and scalar increments (e.g. $\Delta u(r)$) as the Reynolds/Péclet number increased, was followed. This approach is depicted in figure 23 of Mydlarski and Warhaft (1996). These authors chose a single value of r (denoted as r_a in Mydlarski and Warhaft (1996)) that corresponded to the wavenumber κ_1 ($r = 2\pi/\kappa_1$) that lay halfway between the beginning and end of the scaling range for each spectrum. Thus as the scaling range dilated with Reynolds number, r_a, remained in the same relative position within the inertial subrange. Using this approach, the window lengths varied from one case to the next, but always remained in the same relative position on the spectrum, independent of Reynolds number.

Figure 4.6 plots the spectral skewness and kurtosis of the u, v and θ fields using this approach for different Reynolds numbers for window lengths N equal to r_a. Although there are differences in the results when this new methodology is employed to specify the window lengths, the overall (quantitative and qualitative) results and trends in figures 4.3 and 4.6 remain quite similar, thus justifying the robustness of the analysis herein and confirming the relative insensitivity of the effect of window length when the Reynolds number is varied.

4.1.3 Higher-order spectral moments of turbulent scalar fields

Given the different nature of scalar fields (Holzer & Siggia, 1994; Pumir et al., 1991; Warhaft, 2000), it is of particular interest to study the relative levels of intermittency of both velocity and passive scalar fields. To this end, a preliminary analysis (not shown) concluded that a window length of $N = 220\eta$ captured the

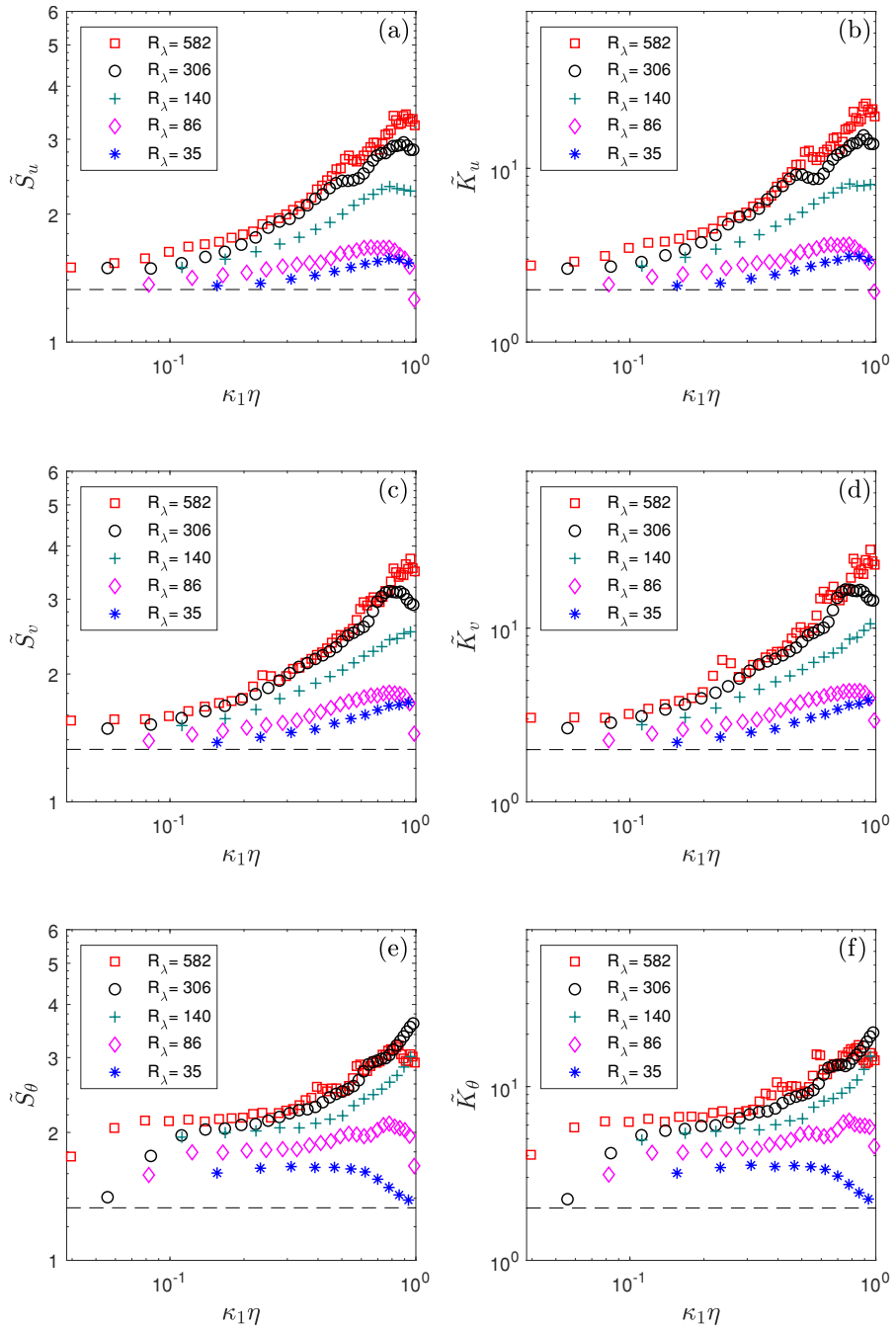

Figure 4.6: Spectral skewness (a, c, e) and kurtosis (b, d, f) of the longitudinal velocity fluctuations u (a, b), the transverse velocity fluctuations v (c, d), and the scalar (temperature) fluctuations θ (e, f) at R_λ = 35 (∗), R_λ = 86 (◇), R_λ = 140 (+), R_λ = 306 (∘), and R_λ = 582 (□). Results are obtained using window lengths corresponding to the midpoint of the inertial subrange.

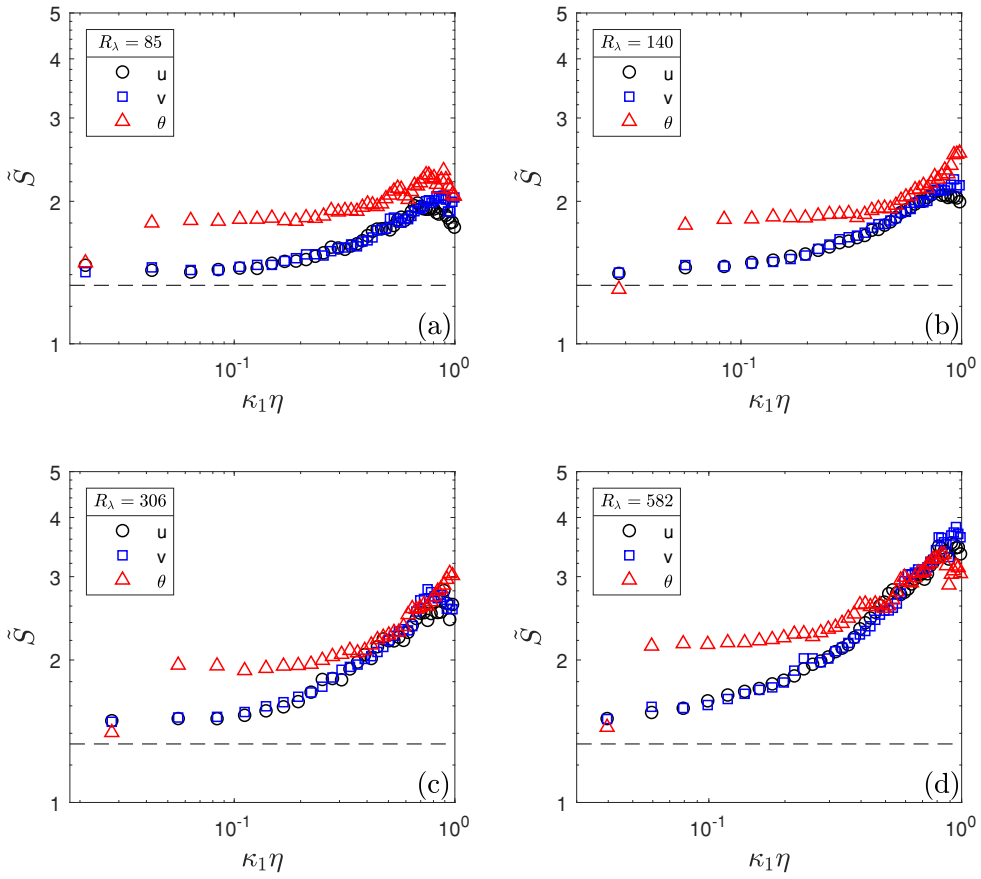

Figure 4.7: Spectral skewness of the longitudinal velocity fluctuations u (○), transverse velocity fluctuations v (□), and scalar (temperature) fluctuations θ (△) at (a) R_λ = 85, (b) R_λ = 140, (c) R_λ = 306, and (d) R_λ = 582. Results are obtained using a window length $N = 220\eta$.

signal transients while also fully capturing frequencies in the dissipation range and most of the inertial-convective subrange.

Plots of the spectral skewness and kurtosis of u, v, and θ are given in figures 4.7 and 4.8, respectively. The overall behaviour of all higher-order spectral moments is similar for all three quantities. More specifically, the curves all show a significant departure from Gaussian behaviour at small scales, and both the spectral skewness and kurtosis exhibit a higher degree of internal intermittency in the inertial-convective

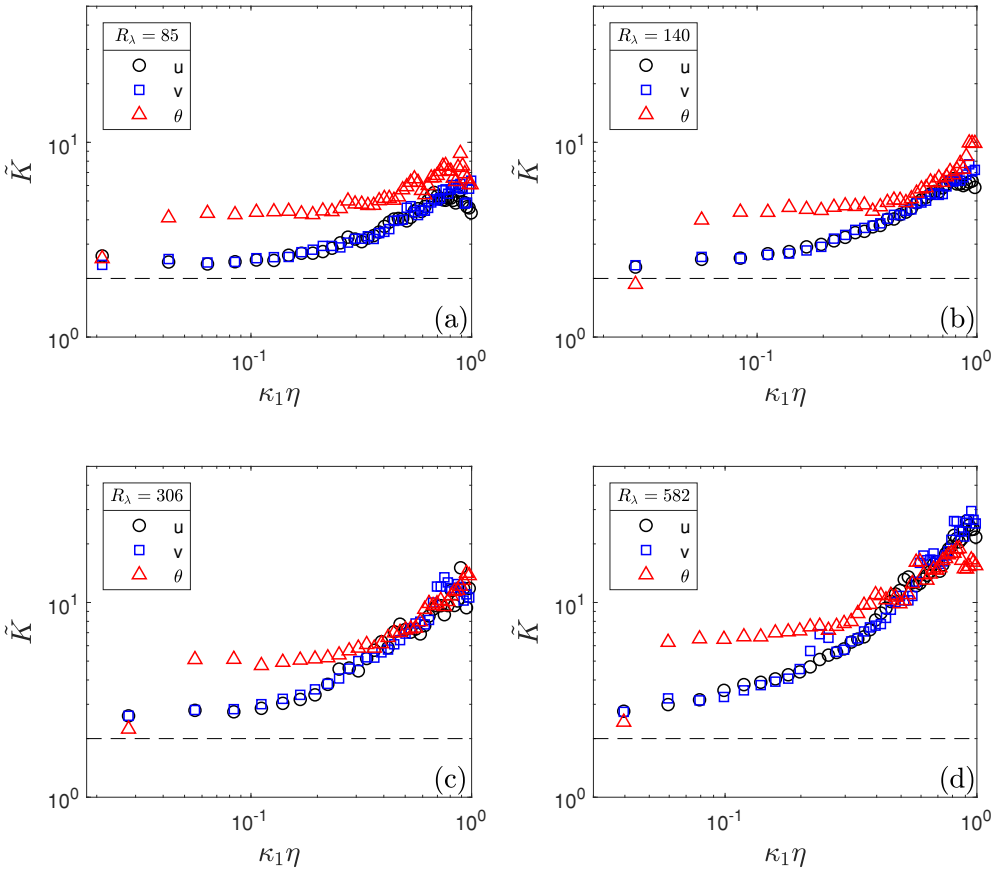

Figure 4.8: Spectral kurtosis of the longitudinal velocity fluctuations u (○), transverse velocity fluctuations v (□), and scalar (temperature) fluctuations θ (△) at (a) R_λ = 85, (b) R_λ = 140, (c) R_λ = 306, and (d) R_λ = 582. Results are obtained using a window length $N = 220\eta$.

subrange for passive scalar fields (compared to the longitudinal and transverse velocity fields, which are both very similar in magnitude in the inertial subrange). Note that these results are consistent with those of Mydlarski and Warhaft (1998), who used the velocity and scalar intermittency exponent to show that scalar fields were more intermittent in the inertial subrange and that their level of intermittent activity increased with Reynolds number. Moreover, they also showed that the level of

intermittency of passive scalar fields remains higher than that of velocity fields at all Reynolds numbers.

The results presented in figures 4.7 and 4.8 show that the spectral skewness and spectral kurtosis of the scalar fluctuations remain at a higher level at small scales (high wavenumbers) when compared to the longitudinal and transverse velocity statistics for the two lower R_λ cases shown. However, the spectral skewness and spectral kurtosis of the longitudinal and transverse velocity fluctuations undergo a rapid increase in the dissipation range and reach levels similar to that of the passive scalar field as $\kappa_1\eta \rightarrow 1$ for the two higher R_λ cases. This suggests that passive scalar fields are more intermittent in the inertial-convective subrange and in part of the dissipation range, but the degree of intermittency of the streamwise and transverse velocity fields becomes similar to that of the scalar field as the Kolmogorov length scale is approached at high Reynolds numbers. This is consistent with the remarks made in §4.1.2 regarding the wavenumber dependence of the Reynolds number evolution of higher-order spectral moments. The plots of figure 4.5 showed that dependence of higher-order spectral moments on Reynolds number was stronger for the velocity field than the passive scalar field at high wavenumbers. This is the reason figures 4.7 and 4.8 show that the higher-order spectral moments of both components of the velocity field reach levels similar to those of the passive scalar field at high wavenumbers for the two highest R_λ cases.

4.2 Higher-order spectral moments in a wall-bounded flow

Previous sections of this thesis demonstrated the ability of higher-order spectral moments to quantify and situate (in the frequency/wavenumber domain) internal intermittency in homogeneous, isotropic, grid-generated turbulence. In this section,

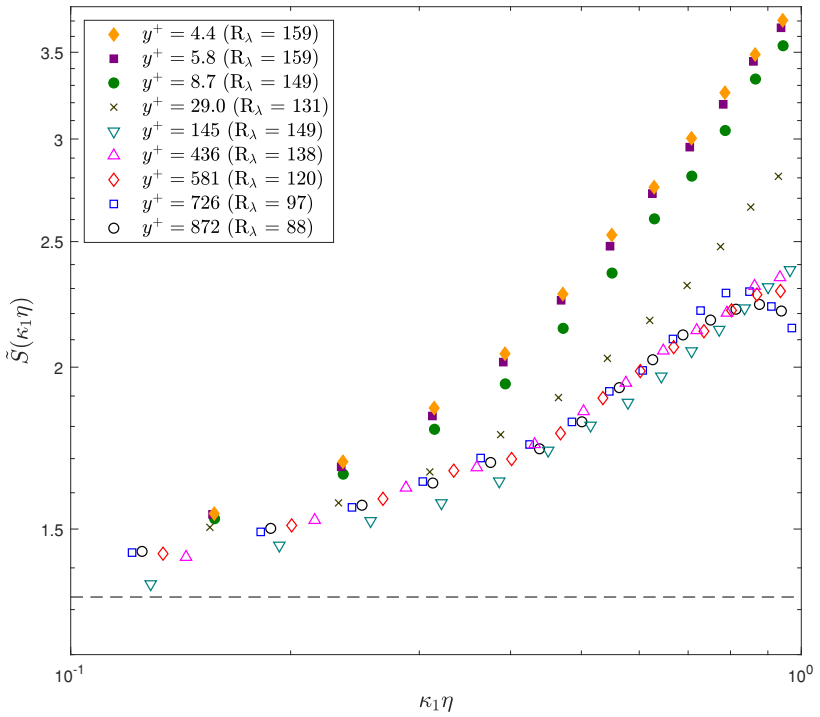

Figure 4.9: Spectral skewness of the longitudinal velocity fluctuations (u) measured in a wall-bounded (channel) flow in the near-wall region (closed symbols) and in the outer layer (open symbols). The measurements were made at wall-normal positions of y^+ = 4.4 (◆), y^+ = 5.8 (■), y^+ = 8.7 (●), y^+ = 29.0 (×), y^+ = 145 (▽), y^+ = 436 (△), y^+ = 581 (◇), y^+ = 726 (□), and y^+ = 872 (○). Results are obtained using a window length $N = 75\eta$. The friction Reynolds number is R_τ = 860 and the local turbulent Reynolds numbers (R_λ) are given in the legend.

higher-order spectral moments are used to investigate intermittent behaviour in wall-bounded flows, which can be approximately homogeneous and isotropic in the outer layer, but inhomogeneous and anisotropic in the near-wall region (Danaila et al., 2001). The results obtained in a wall-bounded flow presented herein were obtained from data taken in the high-aspect-ratio channel of the Aerodynamics Laboratory at McGill University.

The evolution of the spectral skewness and kurtosis in the wall-normal (y) direction of the channel are shown in figures 4.9 and 4.10, respectively. The higher-order

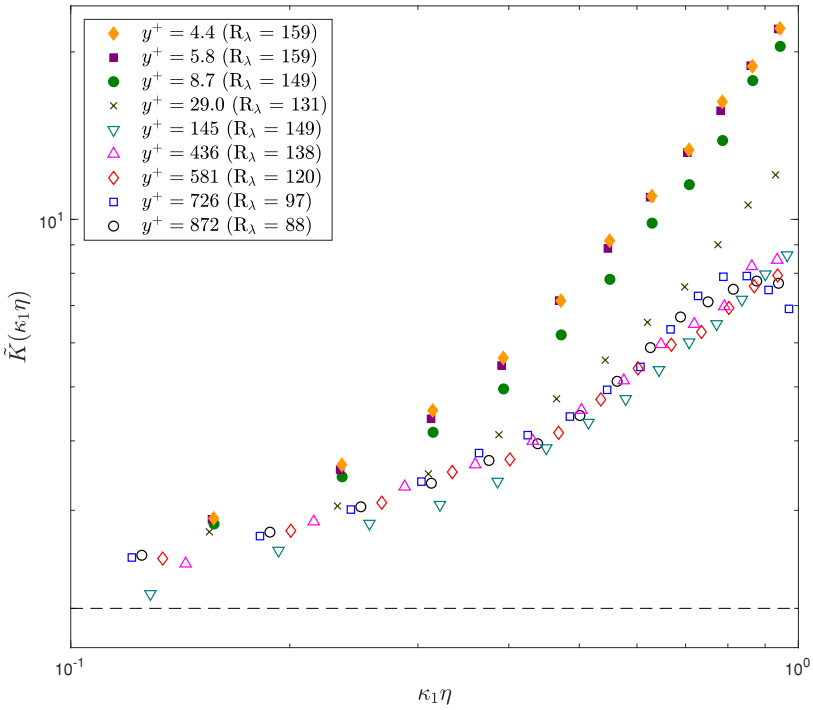

Figure 4.10: Spectral kurtosis of the longitudinal velocity fluctuations (u) measured in a wall bounded (channel) flow in the near wall region (closed symbols) and in the outer layer (open symbols). The measurements were made at wall-normal positions of $y^+ = 4.4$ (◆), $y^+ = 5.8$ (■), $y^+ = 8.7$ (●), $y^+ = 29.0$ (×), $y^+ = 145$ (▽), $y^+ = 436$ (△), $y^+ = 581$ (◇), $y^+ = 726$ (□), and $y^+ = 872$ (○). Results are obtained using a window length $N = 75\eta$. The friction Reynolds number is $R_\tau = 860$ and the local turbulent Reynolds numbers (R_λ) are given in the legend.

spectral moments are obtained using a window length of $N = 75\eta$, where η is calculated at each wall-normal location to eliminate any bias induced by varying window lengths. Note that, in both figures, one observes two distinct clusters of intermittent activity. The first, lower activity group (represented by the open symbols) corresponds to measurements made in the outer layer. All spectral skewness and kurtosis curves in this group have similar shapes and peak levels at high wavenumbers. An increase in the spectral skewness and kurtosis is observed for wall-normal positions $y^+ \leq 29.0$ and a distinct increase is clearly visible at higher wavenumbers for the

measurements made even closer to the wall (closed symbols, $y^+ < 9$), even at locations where the (local) Reynolds number is similar to that farther away from the wall. For example, the Reynolds number of the measurements at $y^+ = 8.7$ matches that of those at $y^+ = 145$, even though the spectral skewness and kurtosis curves exhibit significantly higher levels of intermittent activity at $y^+ = 8.7$. Given the similarity in the Reynolds numbers and window length (in terms of η) at this location, the observed differences provide insights into the inhomogeneous and anisotropic nature of wall-bounded flows in the near-wall region, and cannot be solely attributed to Reynolds number effects. Moreover, the differences in spectral skewness and kurtosis increase as the Kolmogorov length scale is approached ($\kappa_1\eta \rightarrow 1$). The results therefore suggest that the differences in deviations from Gaussian behaviour between the near-wall region and the outer layer become more significant as wavenumber is increased.

The discrepancies between the higher-order spectral moments obtained using measurements made in the near wall region of the channel and those made in homogeneous, isotropic turbulence (either in the outer layer of the channel or in grid-generated turbulence) are likely caused by the presence of intermittent coherent structures such as streaks (discussed in §1.2.4) in the near-wall region. The bursting process that streaks undergo has been shown to be highly intermittent (Robinson, 1991). The results presented in figures 4.9 and 4.10 suggest that the increase in intermittent activity caused by the presence of coherent structures in the near-wall region becomes more significant as the Kolmogorov length scale is approached ($\kappa_1\eta \rightarrow 1$). The higher-order spectral moments therefore are also capable of detecting coherent structures that are not caused by internal intermittency and locate their intermittent activity in wavenumber space. This is an interesting application of higher-order

spectral moments as it provides a novel way to quantitatively analyse near-wall coherent structures, which were historically studied through other methods, including qualitative methods (e.g. flow visualization), conditional sampling methods (e.g. Wallace, Eckelmann, and Brodkey (1972) and Wallace (2016)) and direct numerical simulations (e.g. Bae and Lee (2021)).

CHAPTER 5
Conclusions

5.1 Review of the research and contributions

Chapter 1 of this thesis provided some background information about turbulent flows and their intermittency in addition to reviewing the existing literature on internal intermittency and the detection of transient behaviour. Chapter 1 also set four objectives for the present work:

1. To develop a short-time-Fourier-transform- (STFT-) based method that makes use of higher-order spectral moments to quantify the internal intermittency in the frequency/wavenumber domain,
2. To make use of higher-order spectral moments to explore the Reynolds-number dependence of the internal intermittency of both velocity and passive scalar fields,
3. To compare the intermittency of both velocity and passive scalar fields on a spectral basis,
4. To investigate the use of higher-order spectral moments in wall-bounded flows by comparing the levels of intermittent activity at different wall-normal locations in a turbulent channel flow.

Chapter 2 of this thesis addressed the first objective above by first presenting an overview of the theory behind the third- and fourth-order spectral moments. Then, a short-time-Fourier-transform-based estimator was used to develop an algorithm capable of calculating higher-order spectral moments. The estimator was validated

using Gaussian and non-Gaussian test signals, and the dependence of the estimator on window length was investigated. It was demonstrated that higher-order spectral moments can be used to situate intermittency in wavenumber space and compare the relative levels of intermittency at different scales.

Chapter 3 presented the experimental apparatus used for this research, including a discussion of hot-wire anemometry and the calibration procedure for hot-wire probes. The flow parameters for the wind-tunnel and channel flow fields were tabulated and a detailed discussion of the channel flow facility was given in this chapter.

Chapter 4 of this work addressed the remainder of the objectives given above. The second objective was achieved by first analysing the higher-order spectral moments of turbulent velocity and passive scalar fields. These were shown to exhibit repeatable behaviours, asymptotically approaching Gaussian values at large scales and departing from Gaussian behaviour in the inertial subrange, reaching their maximum values at the smallest scales of the dissipation range. Additionally, it was demonstrated that higher-order spectral moments are Reynolds number dependent. The spectral kurtoses of the longitudinal and transverse velocity fields at $\kappa_1\eta = 0.2$ were found to increase as $\tilde{K}_u(\kappa_1\eta = 0.2) \sim R_\lambda^{0.3}$, which is consistent with the behaviour of the overall kurtosis of velocity derivatives observed by Van Atta and Antonia (1980). Moreover, the Reynolds number dependence of the higher-order spectral moments was shown to depend on wavenumber. The third objective was addressed by comparing the magnitude and wavenumber dependence of the internal intermittency of passive scalar fields to that of velocity fields using the spectral skewness and kurtosis. The results revealed that the level of intermittency of passive scalar fluctuations is higher in the inertial subrange and part of the dissipation

range when compared to those of the longitudinal and transverse velocity fluctuations. However for the higher R_λ cases and as $\kappa_1\eta \rightarrow 1$, the levels of intermittency of the longitudinal and transverse velocity fluctuations were seen to increase rapidly and eventually become similar to those of the passive scalar field. Finally, the fourth objective was achieved by analysing the higher-order spectral moments of velocity measurements made in the channel of the Aerodynamics Laboratory. The results revealed increased intermittent activity in the near-wall region of the wall bounded flow, attributed to the presence of coherent motions (e.g. streaks) that undergo an intermittent process often referred to as "bursting." The increase in intermittent activity caused by the presence of coherent structures was seen to become more significant as the Kolmogorov length scale was approached. Higher-order spectral moments were thus shown to offer a way to quantify and locate the intermittent activity of coherent structures in wavenumber space.

5.2 Future work

The results herein suggest that our knowledge of internal intermittency can be expanded by way of higher-order spectral moments. Future work shall be primarily aimed at comparing the wavenumber dependence and levels of intermittency between different classes of flows. This research has shown that higher-order spectral moments are well suited to the study intermittent phenomena, and it is therefore hoped that they can be used to investigate additional turbulence phenomena, such as coherent structures in free-shear flows such as turbulent wakes. Additional measurements of transverse velocity and passive scalar fields in wall-bounded flows should also be made to analyse the effects of coherent structures on these quantities by way of higher-order spectral moments.

A better understanding of the the way the higher-order spectral moments of velocity and passive scalar fields compare may also be achieved by obtaining similar measurements at higher Reynolds numbers. This research has shown that the higher-order spectral moments of both velocity and passive scalar field tend to similar levels in the dissipation range and as the Reynolds number is increased. However, additional measurements taken at even higher Reynolds numbers (e.g. in the atmospheric boundary layer) may help confirm this trend.

APPENDIX A
Derivation of Gaussian values of higher-order spectral moments

The raw moments of the chi distribution, which arises from the magnitude of complex Fourier transforms, may be calculated from equation 2.7 by integrating the following product:

$$\mu_j = \langle X^j \rangle = \int_{-\infty}^{\infty} X^j \frac{2^{1-L/2} X^{L-1}}{\Gamma(L/2)\sigma^L} \mathrm{e}^{-X^2/2\sigma^2} dX. \tag{A.1}$$

Given that $X \geq 0$ (because of the squaring operation necessary to obtain the magnitude of the complex number), the integration bounds may be changed to:

$$\mu_j = \langle X^j \rangle = \int_{0}^{\infty} X^j \frac{2^{1-L/2} X^{L-1}}{\Gamma(L/2)\sigma^L} \mathrm{e}^{-X^2/2\sigma^2} dX. \tag{A.2}$$

This integral is of the form:

$$\int_0^{\infty} x^m \mathrm{e}^{-ax^2} dx, \tag{A.3}$$

with $a = 1/2\sigma^2$ and $m = j + L - 1$. The general solution to this integral is (Spiegel, Lipschutz, & Liu, 2018):

$$\int_0^{\infty} x^m \mathrm{e}^{-ax^2} dx = \frac{\Gamma((m+1)/2)}{2a^{(m+1)/2}}. \tag{A.4}$$

Therefore, the raw moments of the chi distribution are obtained by solving equation A.1 using equation A.4:

$$\mu_j = \frac{2^{1-L/2}}{\Gamma(L/2)\sigma^L} \frac{\Gamma((m+1)/2)}{2a^{(m+1)/2}}, \tag{A.5}$$

which simplifies to:

$$\mu_j = \sigma^j 2^{j/2} \frac{\Gamma(\frac{1}{2}(L+j))}{\Gamma(\frac{1}{2}L)}. \tag{A.6}$$

Therefore, for a Gaussian signal, the proposed definitions of higher-order spectral moments lead to a spectral skewness of:

$$\tilde{S} = \frac{\mu_3}{\mu_2^{3/2}} = \frac{\sigma^3 2^{3/2} \frac{\Gamma(\frac{1}{2}(2+3))}{\Gamma(\frac{1}{2}2)}}{\left[\sigma^2 2^{2/2} \frac{\Gamma(\frac{1}{2}(2+2))}{\Gamma(\frac{1}{2}2)}\right]^{3/2}} = \frac{\Gamma(5/2)}{[\Gamma(2)]^{3/2}} = \Gamma(5/2) = 1.3293, \tag{A.7}$$

and a spectral kurtosis of:

$$\tilde{K} = \frac{\mu_4}{\mu_2^2} = \frac{\sigma^4 2^{4/2} \frac{\Gamma(\frac{1}{2}(2+4))}{\Gamma(\frac{1}{2}2)}}{\left[\sigma^2 2^{2/2} \frac{\Gamma(\frac{1}{2}(2+2))}{\Gamma(\frac{1}{2}2)}\right]^2} = \frac{\Gamma(3)}{[\Gamma(2)]^2} = \Gamma(3) = 2. \tag{A.8}$$

The aforementioned results apply to a random variable created by taking the square root of the sum of the square of two independent random variables. However, for a Fourier transform calculated at any frequency $\omega_n = 2\pi n f_s/2$, $n = 0, 1, 2, ...$, the imaginary part vanishes and taking the magnitude is equivalent to simply taking the absolute value of a single variable (X^r). Therefore, in this case, the magnitude of the Fourier transform of a Gaussian signal yields a half-normal distribution with probability density function

$$f(X|\sigma, L) = \frac{\sqrt{2}}{\sigma\sqrt{\pi}} \mathrm{e}^{-X^2/2\sigma^2} \tag{A.9}$$

instead of a chi distribution. The raw moments of this distribution can be calculated from:

$$\mu_j = \langle X^j \rangle = \int_{-\infty}^{\infty} X^j \frac{\sqrt{2}}{\sigma\sqrt{\pi}} \mathrm{e}^{-X^2/2\sigma^2} dX, \tag{A.10}$$

which may, again, be solving using a general solution of the form A.4, yielding:

$$\mu_j = \frac{(\sigma\sqrt{2})^j}{\sqrt{\pi}}\Gamma(\frac{1}{2}(j+1)). \tag{A.11}$$

Therefore, the spectral skewness of a Gaussian signal at $\omega_n = 2\pi n f_s/2$, $n = 0, 1, 2, ...$ becomes:

$$\tilde{S} = \frac{\mu_3}{\mu_2^{3/2}} = \frac{\frac{(\sigma\sqrt{2})^3}{\sqrt{\pi}}\Gamma(\frac{1}{2}(3+1))}{\left(\frac{(\sigma\sqrt{2})^2}{\sqrt{\pi}}\Gamma(\frac{1}{2}(2+1))\right)^{3/2}} = \frac{\frac{(\sigma\sqrt{2})^3}{\sqrt{\pi}}}{\left(\frac{(\sigma\sqrt{2})^2}{\sqrt{\pi}}\frac{1}{2}\sqrt{\pi}\right)^{3/2}} = \sqrt{\frac{8}{\pi}} = 1.5958, \tag{A.12}$$

and the spectral kurtosis becomes

$$\tilde{K} = \frac{\mu_4}{\mu_2^2} = \frac{\frac{(\sigma\sqrt{2})^4}{\sqrt{\pi}}\Gamma(\frac{1}{2}(4+1))}{\left(\frac{(\sigma\sqrt{2})^2}{\sqrt{\pi}}\Gamma(\frac{1}{2}(2+1))\right)^2} = \frac{\frac{3(\sigma\sqrt{2})^4}{4}}{\left(\frac{(\sigma\sqrt{2})^2}{\sqrt{\pi}}\frac{1}{2}\sqrt{\pi}\right)^2} = 3. \tag{A.13}$$

This change in distribution causes a jump in the spectral skewness and kurtosis values at $\omega_n = 2\pi n f_s/2$, $n = 0, 1, 2, ...$ The periodic nature of the Fourier transform causes this jump to occur cyclically, though for practical purposes it is only observed at a frequency corresponding to half the sampling frequency ($\omega_n = 2\pi f_s/2$) as the other repeated Fourier coefficients are rarely plotted. Because of window leakage (Press et al., 1986), this discontinuity spreads to neighbouring Fourier modes. Therefore, the algorithm developed for this research includes a correction factor (based on that of Antoni (2006)) that eliminates the effects of this discontinuity.

APPENDIX B
Uncertainty and error analysis

The purpose of this appendix is to analyse the various sources of uncertainty that arise from the measurement and calculation of turbulent velocity statistics that were undertaken by the author in the turbulent channel flow facility in the McGill University Aerodynamics Laboratory. According the guidelines given by Tavoularis (2005), there are two distinct categories of of uncertainty: (i) bias error and (ii) precision error. Bias error (denoted by b) is systematic and representative the accuracy of the measurements. For the present analysis, bias error is assumed to correspond to the accuracy of the equipment as specified by the manufacturer. Precision error (denoted by p) is associated with the repeatability of the measurements. Precision errors may be estimated in one of two ways, depending on their type. The types of precision errors and their respective estimation methods are as follows:

- Type 1 precision errors arise from time series of N measurements with mean μ and standard deviation σ. For these types of errors, Tavoularis (2005) recommend calculating the precision error (p) using:

$$p = \frac{2\sigma}{\sqrt{N}}. \tag{B.1}$$

- Type 2 precision errors arise from single point measurements. Given an instrument with a precision of σ, the error is assumed to be uniformly distributed, yielding a precision error of:

$$p = \frac{\sigma}{\sqrt{3}}. \tag{B.2}$$

Using the precision and bias errors of each source of error, the total measurement uncertainty (u) can be calculated as (Tavoularis, 2005):

$$u = \sqrt{\sum_i b_i^2 + \sum_i p_i^2}. \tag{B.3}$$

The following sections will present the uncertainties that arise from velocity measurements and turbulent statistics. This is followed by an overview of the errors related to the hot-wire probe's temporal and spatial resolution.

B.1 Velocity measurement uncertainty

Errors associated with the velocity measurements presented herein generally arise from (i) the calibration measurements, (ii) the DAQ board, and (iii) the curve fits to the calibration data. This section begins with an analysis of the the uncertainty that arises from the calibration. The total uncertainty on the instantaneous velocity measurements are then calculated.

B.1.1 Calibration apparatus error

The calibration jet outputs the differential pressure between the settling chamber and the ambient pressure (which is equal to the pressure of the jet of air flowing out of the calibration apparatus). Knowledge of the differential pressure, the stagnation temperature, and the ambient pressure allows one to establish the velocity at the jet exit using isentropic relations. A summary of the errors that arise from the differential pressure measurements, the ambient pressure measurements, and the temperature measurements is presented in table B–1.

The differential pressure readings are recorded by the A/D DAQ board. The error that arises from the A/D DAQ board (u_E) is the combination of the bias and

Error source	Description	Type	σ	b_i or p_i
A/D DAQ board	Accuracy of PCI-6143 A/D DAQ board	Bias	N/A	±3.613 mV
	Precision of PCI-6143 A/D DAQ board	Precision type 2	0.153 mV	±0.0883 mV
Mercury barometer	Precision of pressure reading	Precision type 2	0.10 mmHg	±0.060 mmHg
Thermocouple	Accuracy of the Type E thermocouple	Bias	N/A	±1.7 K
	Precision of the thermocouple display	Precision type 2	0.1 K	±0.06 K

Table B–1: Summary of the sources of error associated with the calibration of a hot-wire probe.

precision errors (see table B–1 for the values):

$$u_E = \sqrt{(3.613 \text{ mV})^2 + (0.0883 \text{ mV})^2} = 3.614 \text{ mV}. \tag{B.4}$$

The differential pressure readings produced by the pressure transducer correspond to voltages of 0 V to 10 V for pressure differences of 0 mmHg to 100 mmHg. Assuming a linear relation between voltage and pressure, the uncertainty associated with differential pressure measurements ($u_{\Delta p}$) is estimated from:

$$u_{\Delta p} = \sqrt{\left(\frac{\partial(\Delta p)}{\partial E} u_E\right)^2}, \tag{B.5}$$

which yields $u_{\Delta p} = 0.03614$ mmHg. Moreover, the ambient pressure uncertainty (u_p) arises from the mercury barometer readings, and thus, from table B–1, $u_p = 0.060$ mmHg. Finally, the error from the temperature measurements correspond to a combination of the bias and precision error (see table B–1 for the values), such that:

$$u_T = \sqrt{(1.7 \text{ K})^2 + (0.06 \text{ K})^2} = 1.7 \text{ K}. \tag{B.6}$$

Error source	Description	Type	σ	b_i or p_i
A/D DAQ board	Accuracy of PCI-6143 A/D DAQ board	Bias	N/A	±3.613 mV
	Precision of PCI-6143 A/D DAQ board	Precision type 2	0.153 mV	±0.0883 mV
Calibration measurements	Refer to §B.1.1	Precision and bias	N/A	±0.29 m/s
Curve fit	Error in velocity calibration curve fit	Bias	N/A	±0.0135 m/s

Table B–2: Summary of the sources of error associated with instantaneous velocity measurements.

Given measurements of differential pressure, ambient pressure, and temperature, the velocity of the jet can be calculated from the isentropic relations for compressible flow. The uncertainty on the calibration velocity data points can therefore be calculated from:

$$u_{calib} = \sqrt{\left(\frac{\partial U}{\partial(\Delta p)}u_{\Delta p}\right)^2 + \left(\frac{\partial U}{\partial p}u_p\right)^2 + \left(\frac{\partial U}{\partial T}u_T\right)^2}, \tag{B.7}$$

where the partial derivatives $\partial U/\partial(\Delta p)$, $\partial U/\partial p$, and $\partial U/\partial T$ are estimated from the isentropic relations. Equation B.7 therefore yields a calibration uncertainty of:

$$u_{calib} = 0.29 \text{ m/s} \tag{B.8}$$

B.1.2 Instantaneous velocity measurement uncertainty

As previously mentioned, the total error on the instantaneous velocity measurements arises from three sources: (i) the calibration measurements, (ii) the DAQ board, and (iii) the curve fits to the calibration data. The uncertainty values associated with the total error on the instantaneous velocity measurements are summarised in table B–2.

The uncertainty associated with the A/D DAQ board is the combination of the bias and precision uncertainties. This value was already calculated in equation B.4, which yielded: $u_E = 3.614$ mV. Additionnally, for a single-normal hot-wire, the partial derivative that enables one to translate this uncertainty in voltage to an uncertainty in velocity is estimated from Kings's Law to be $\frac{\partial U}{\partial E} = 12.5$ m/(sV). Moreover, the uncertainty arising from the calibration curve-fit is estimated as follows for a single-normal hot wire:

$$u_{fit} = \sqrt{\frac{1}{N-3}\sum_{i-1}^{N}(U_m - U_{fit})^2}, \tag{B.9}$$

where U_m is the measured velocity and U_{fit} is the velocity obtained from the curve fit. For the calibration used herein, the calibration curve-fit uncertainty is $u_{fit} = 0.0135$ m/s.

Combining the three sources of error from table B–2, the total uncertainty on the velocity measurements is:

$$u_U = \sqrt{\left(\frac{\partial U}{\partial E}u_E\right)^2 + u_{calib}^2 + u_{fit}^2}, \tag{B.10}$$

which yields $u_U = 0.29$ m/s, indicating the uncertainty in the calibration is the dominant one.

B.2 Uncertainty of turbulent statistics

The previous section estimated errors in instantaneous velocity measurements, though most of the turbulent statistics quoted herein are obtained from fluctuating quantities (i.e. $u = U - \langle U \rangle$). Tavoularis (2005) states that, for quantities calculated using differences measured using the same instruments, the bias error is cancelled out by the subtraction operation. Therefore, to obtain the uncertainty pertaining

to velocity statistics, the process outlined in §B.1 is repeated, setting to zero all uncertainties related to bias errors. The resulting uncertainty associated with the velocity statistics is therefore $u_{\Delta U}$ = 0.0012 m/s.

B.3 Hot-wire probe temporal and spatial resolution errors

The temporal resolution of hot-wire probes is determined by the frequency response of the anemometer used with the hot wire probe. The DISA 55M01 constant temperature anemometer used for the velocity measurements in the channel has a maximum frequency response of 200 kHz (depending on the probe and probe cable used). Given that the highest Kolmorogorov length scale frequency recorded herein was close to 12 kHz, the maximum frequency response offered by the DISA 55M01 is more than sufficient for the purposes of this research. The temporal resolution error is therefore assumed to be negligible for the velocity measurements presented herein.

Another source of error is that associated with the spatial resolution of the hot-wire probe, especially for measurements made in the near wall region of the channel. In the viscous sublayer, the Kolmogorov length scale (η) becomes smaller because of the increase in the turbulent kinetic energy dissipation rate (see table 3–2). To adequately measure the velocity fluctuations in this region, the length of the hot-wire should be small enough to resolve length scales on the order of η. In his study on the measurements of small-scale turbulence with hot-wires, Wyngaard (1968) suggested that a Kolmogorov-microscale-to-wire-length ratio (η/ℓ) of 0.35 is sufficient to resolve scales on the order of the Kolmogorov microscale to within 7%. This was taken into consideration while building the hot-wire probe used for the velocity measurements made for this research and the length of the sensing element used herein was approximately three times the size of the smallest Kolmogorov microscale encountered for this research, which closely follows the guideline of η/ℓ = 0.35.

References

Antoni, J. (2006). The spectral kurtosis: a useful tool for characterising non-stationary signals. *Mech. Syst. Signal Pr.*, *20*(2), 282–307.

Antoni, J. (2007). Fast computation of the kurtogram for the detection of transient faults. *Mech. Syst. Signal Pr.*, *21*(1), 108–124.

Antoni, J., & Randall, R. B. (2006). The spectral kurtosis: application to the vibratory surveillance and diagnostics of rotating machines. *Mech. Syst. and Signal Pr.*, *20*(2), 308–331.

Bae, H. J., & Lee, M. (2021). Life cycle of streaks in the buffer layer of wall-bounded turbulence. *Phys. Rev. Fluids*, *6*(6), 064603.

Batchelor, G. K., & Townsend, A. A. (1949). The nature of turbulent motion at large wavenumbers. *P. Roy. Soc. Lond. A Mat.*, *199*(1057), 238–255.

Brun, C., & Pumir, A. (2001). Statistics of fourier modes in a turbulent flow. *Phys. Rev. E*, *63*(5), 056313.

Bruun, H. (1995). *Hot-wire anemometry, principles and signal analysis*. Oxford University Press.

Chevillard, L., Mazellier, N., Poulain, C., Gagne, Y., & Baudet, C. (2005). Statistics of Fourier modes of velocity and vorticity in turbulent flows: Intermittency and long-range correlations. *Phys. Rev. Lett.*, *95*(20), 200203.

Corrsin, S. (1951). On the spectrum of isotropic temperature fluctuations in an isotropic turbulence. *J. Appl. Phys.*, *22*(4), 469–473.

Danaila, L., Anselmet, F., Zhou, T., & Antonia, R. A. (2001). Turbulent energy

scale budget equations in a fully developed channel flow. *J. Fluid Mech.*, *430*, 87–109.

Djenidi, L., Antonia, R. A., & Tang, S. L. (2019). Scale invariance in finite Reynolds number homogeneous isotropic turbulence. *J. Fluid Mech.*, *864*, 244–272.

Dwyer, R. F. (1983). A technique for improving detection and estimation of signals contaminated by under ice noise. *J. Acoust. Soc. Am*, *74*(1), 124–130.

Farge, M. (1992). Wavelet transforms and their applications to turbulence. *Annu. Rev. Fluid Mech.*, *24*(1), 395–458.

Forbes, C., Evans, M., Hastings, N., & Peacock, B. (2011). *Statistical distributions*. John Wiley & Sons.

Holzer, M., & Siggia, E. D. (1994). Turbulent mixing of a passive scalar. *Phys. Fluids*, *6*(5), 1820–1837.

Hu, Y., Bao, W., Tu, X., Li, F., & Li, K. (2019). An adaptive spectral kurtosis method and its application to fault detection of rolling element bearings. *IEEE T. Instrum. Meas.*, *69*(3), 739–750.

Kennedy, D. A., & Corrsin, S. (1961). Spectral flatness factor and 'intermittency' in turbulence and in non-linear noise. *J. Fluid Mech.*, *10*(3), 366–370.

Kline, S. J., Reynolds, W. C., Schraub, F. A., & Runstadler, P. W. (1967). The structure of turbulent boundary layers. *J. Fluid Mech.*, *30*(4), 741–773.

Kolmogorov, A. N. (1941a). Dissipation of energy in the locally isotropic turbulence. *Dokl. Akad. Nauk. SSSR*, *32*, 16–18.

Kolmogorov, A. N. (1941b). The local structure of turbulence in incompressible viscous fluid for very large Reynolds numbers. *Dokl. Akad. Nauk. SSSR*, *30*, 301–305.

Kraichnan, R. H. (1967). Intermittency in the very small scales of turbulence. *Phys.*

Fluids., *10*(9), 2080–2082.

Kraichnan, R. H. (1994). Anomalous scaling of a randomly advected passive scalar. *Phys. Rev. Lett.*, *72*(7), 1016.

Kuo, A. Y., & Corrsin, S. (1971). Experiments on internal intermittency and fine-structure distribution functions in fully turbulent fluid. *J. Fluid Mech.*, *50*(2), 285–319.

Landau, L. D. (1944). On the problem of turbulence. *Dokl. Akad. Nauk. USSR*, *44*, 311.

Lavertu, R. A., & Mydlarski, L. (2005). Scalar mixing from a concentrated source in turbulent channel flow. *J. Fluid Mech.*, *528*, 135.

Leite, V. C., Borges da Silva, J. G., Borges da Silva, L. E., Veloso, G. F. C., Lambert-Torres, G., Bonaldi, E. L., & de Oliveira, L. E. L. (2016). Experimental bearing fault detection, identification, and prognosis through spectral kurtosis and envelope spectral analysis. *Electr. Pow. Compo. and Sys.*, *44*(18), 2121–2132.

Lepore, J., & Mydlarski, L. (2012). Finite-Péclet-number effects on the scaling exponents of high-order passive scalar structure functions. *J. Fluid Mech.*, *713*, 453.

Lumley, J. (1965). Interpretation of time spectra measured in high-intensity shear flows. *Phys. Fluids.*, *8*(6), 1056–1062.

Makita, H. (1991). Realization of a large-scale turbulence field in a small wind tunnel. *Fluid Dyn. Res.*, *8*(1-4), 53.

Mehta, R. D., & Bradshaw, P. (1979). Design rules for small low speed wind tunnels. *Aeronaut. J.*, *83*(827), 443–453.

Meneveau, C. (1991). Analysis of turbulence in the orthonormal wavelet representation. *J. Fluid Mech.*, *232*, 469–520.

Meyer, C. R., Mydlarski, L., & Danaila, L. (2018). Statistics of incremental averages of passive scalar fluctuations. *Phys. Rev. Fluids*, *3*(9), 094603.

Millioz, F., Huillery, J., & Martin, N. (2006). Short time Fourier transform probability distribution for time-frequency segmentation. *Int. Conf. Acoust. Spee.*, *3*, III–III.

Mydlarski, L. (2017). A turbulent quarter century of active grids: from Makita (1991) to the present. *Fluid Dyn. Res.*, *49*(6), 061401.

Mydlarski, L., & Warhaft, Z. (1996). On the onset of high-Reynolds-number grid-generated wind tunnel turbulence. *J. Fluid Mech.*, *320*, 331–368.

Mydlarski, L., & Warhaft, Z. (1998). Passive scalar statistics in high-Péclet-number grid turbulence. *J. Fluid Mech.*, *358*, 135–175.

Oboukhov, A. M. (1949). Structure of the temperature field in turbulent flows. *Akad. Nauk. SSSR*, *13*, 58–69.

Pagnan, S., & Ottonello, G., C.and Tacconi. (1994). Filtering of randomly occurring signals by kurtosis in the frequency domain. In *Int. c. patt. recog.* (pp. 131–133).

Peligrad, M., & Wu, W. B. (2010). Central limit theorem for Fourier transforms of stationary processes. *Ann. Prob.*, *38*(5), 2009–2022.

Pope, S. (2000). *Turbulent flows*. Cambridge University Press.

Press, W. H., Teukolsky, S. A., Vetterling, W., & Flannery, B. P. (1986). *Numerical recipes in FORTRAN 77*. Cambridge University Press.

Pumir, A., Shraiman, B. I., & Siggia, E. D. (1991). Exponential tails and random advection. *Phys. Rev. Lett.*, *66*(23), 2984.

Richardson, L. F. (1922). *Weather prediction by numerical process.* Cambridge university press.

Robinson, S. K. (1991). Coherent motions in the turbulent boundary layer. *Annu. Rev. Fluid. Mech.*, *23*(1), 601–639.

Spiegel, M. R., Lipschutz, S., & Liu, J. (2018). *Schaum's mathematical handbook of formulas and tables* (5th ed.).

Sreenivasan, K. R., & Antonia, R. A. (1997). The phenomenology of small-scale turbulence. *Annu. Rev. Fluid Mech.*, *29*(1), 435–472.

Tavoularis, S. (2005). *Measurement in fluid mechanics.* Cambridge University Press.

Taylor, G. I. (1935). Statistical theory of turbulence: Parts I-III. *Proc. R. Soc. London Ser. A*, *151*, 421–464.

Tennekes, H., & Lumley, J. L. (1972). *A first course in turbulence.* MIT press.

Van Atta, C. W., & Antonia, R. A. (1980). Reynolds number dependence of skewness and flatness factors of turbulent velocity derivatives. *Phys. Fluids*, *23*(2), 252–257.

Wallace, J. M. (2016). Quadrant analysis in turbulence research: history and evolution. *Annu. Rev. Fluid Mech.*, *48*, 131–158.

Wallace, J. M., Eckelmann, H., & Brodkey, R. S. (1972). The wall region in turbulent shear flow. *J. Fluid Mech.*, *54*(1), 39–48.

Warhaft, Z. (2000). Passive scalars in turbulent flows. *Annu. Rev. Fluid Mech.*, *32*(1), 203–240.

Welch, P. (1967). The use of fast Fourier transform for the estimation of power spectra: a method based on time averaging over short, modified periodograms. *IEEE T. Acoust. Speech.*, *15*(2), 70–73.

Wyngaard, J. C. (1967). Ph.D. thesis. *University of Pennsylvania.*

Wyngaard, J. C. (1968). Measurement of small-scale turbulence structure with hot wires. *J. Phys. E. Sci. Instrum.*, *1*(11), 1105–1108.